5-2014

Development of a FLUKA-Based Lookup Tool for Rapid Analysis of Radiation Exposures in Space Environments

John Macdougall Brittingham
University of Tennessee - Knoxville, jbritti1@utk.edu

To the Graduate Council:

I am submitting herewith a dissertation written by John Macdougall Brittingham entitled "Development of a FLUKA-Based Lookup Tool for Rapid Analysis of Radiation Exposures in Space Environments." I have examined the final electronic copy of this dissertation for form and content and recommend that it be accepted in partial fulfillment of the requirements for the degree of Doctor of Philosophy, with a major in Nuclear Engineering.

Lawrence W. Townsend, Major Professor

We have read this dissertation and recommend its acceptance:

Lawrence H. Heilbronn, Ronald E. Pevey, Thomas Handler

Accepted for the Council:

Carolyn R. Hodges

Vice Provost and Dean of the Graduate School

(Original signatures are on file with official student records.)

Development of a FLUKA-Based Lookup Tool for Rapid Analysis of Radiation Exposures in Space Environments

A Dissertation Presented for the

Doctor of Philosophy

Degree

The University of Tennessee, Knoxville

John Macdougall Brittingham

May 2014

Dedication

For Deseree, Marin, and Henry

Acknowledgements

I owe a deep debt of gratitude to a number of people who have helped me on this journey. In particular, I would like to acknowledge the invaluable contribution of my adviser Professor Lawrence Townsend who has always helped me when I needed help but given me the leeway I needed to learn how to plan and execute scientific research.

I thank Professors Lawrence Heilbronn, Ronald Pevey, and Thomas Handler for serving on my thesis committee. Professor Pevey's Monte Carlo Analysis course and Professor Heilbronn's Radiation Protection course played a vital role in shaping my professional interest in the field. Professor Heilbronn also helped me understand the detection and measurement of radiation while serving as my adviser for my Master of Science thesis.

Jamie Porter provided me indispensable assistance by answering a seemingly endless barrage of questions regarding the CRaTER instrument and her model of the instrument.

I am grateful to the entire Nuclear Engineering department at the University of Tennessee for its contribution to my education as an engineer. Many other members of the department who are unnamed here have helped me significantly.

Kerry Lee and Janet Barzilla of NASA-JSC SRAG provided significant assistance in the development of my understanding of the FLUKA code.

I thank Art Domby for his understanding and support over the several days of work that I missed in order to pursue this research.

I am indebted to my entire family for their support in this and all of my academic endeavors. In particular, I thank my children Marin and Henry for their patience and understanding when my research encroached on the time that we have to spend together.

I could not have completed my dissertation without the help of my wife Deseree. She has been extraordinarily supportive of me throughout this entire endeavor and has made significant personal sacrifice so that I could finish this work.

Abstract

Monte Carlo transport codes such as FLUKA provide an accurate and effective method to model the transport of space radiation. However, their use in time-sensitive applications is limited because they do not generate results as quickly as other methods, such as deterministic transport codes. The development of a pre-calculated lookup tool for use in complex space radiation environments allows the calculation of space radiation quantities such as dose, dose equivalent, and fluence using Monte Carlo results with minimal loss of accuracy. In this work, a lookup tool suitable for rapidly estimating radiation exposures is developed using the FLUKA Monte Carlo code and then compared to experimental data and other simulations using other codes (HETC-HEDS and HZETRN). Specifically, the FLUKA calculations were compared to experimental data from the Cosmic Ray Telescope for the Effects of Radiation ("CRaTER") instrument, which is carried on the Lunar Reconnaissance Orbiter ("LRO"), as well as to HETC-HEDS and HZETRN calculations simulating CRaTER. These comparisons demonstrate both the usefulness and the limitations of a pre-calculated lookup tool to rapidly model the effects of galactic cosmic radiation and solar particle events. The pre-calculated lookup tool was also used to calculate organ dose equivalent and effective dose behind a large number of shielding combinations.

Table of Contents

List of Tables

List of Figures

List of Abbreviations

CAF	Computerized Anatomical Female
CAM	Computerized Anatomical Male
CRaTER	Cosmic Ray Telescope for the Effects of Radiation
GCR	Galactic Cosmic Radiation
LEO	Low-Earth Orbit
LET	Linear Energy Transfer
LRO	Lunar Reconnaissance Orbiter
MSL	Mars Space Laboratory
NASA	National Aeronautics and Space Administration
PEL	Permissible Exposure Limit
RAD	Radiation Assessment Detector
REID	Risk of Exposure-Induced Death
SPE	Solar Particle Event
SRAG	Space Radiation Analysis Group
TEP	Tissue-Equivalent Plastic

I. Introduction

A. Motivation

The exposure of personnel and equipment to space radiation is a substantial barrier to the continued exploration of space. The 2011 National Aeronautics and Space Administration ("NASA") Strategic Plan (Ref. 1) Strategic Goal 1.3 aims to "[d]evelop an integrated architecture and capabilities for safe crewed and cargo missions beyond low Earth orbit." Within NASA's Space Technology Roadmap, this research most directly contributes to Technical Area Six (TA06), which is entitled "Human Health, Life Support, and Habitation Systems" (Ref. 2). In this Technology Area, "[t]he radiation area is focused on developing knowledge and technologies to understand and quantify radiation health and performance risks, to develop mitigation countermeasures, and to minimize exposures through the use of material shielding systems."

In its planning for a possible manned mission to Mars, NASA is considering missions that will last 600 to 900 days. Current technology allows for manned missions beyond low-earth orbit ("LEO") for 90 to 100 days before the Permissible Exposure Limit ("PEL") is exceeded. NASA estimates that a mission of longer duration will likely result in three to five times the PEL. NASA recognizes that feasible shielding configurations will not likely be able to bring doses within PELs for longer missions, so NASA's current challenge for the radiation area is to reduce astronaut GCR exposure by 20 to 30% by "optimiz[ing] multi-functional shielding systems" (Ref. 2).

Obtaining accurate and timely estimates of the radiological damage caused by galactic cosmic radiation ("GCR") and solar particle events ("SPE") is vital to meeting the technology challenge of manned spaceflight beyond LEO. Estimating the amount and biological effects of space radiation is complicated by the attenuation of the radiation by the spacecraft, installed shielding, and body self-shielding. Space radiation interacts with the shielding materials, so the character and energy of the radiation that causes a biological effect can be quite different from the character and energy of the radiation that is incident on the spacecraft.

The use of the Monte Carlo method increases the predictive power of current models for the biological and equipment damage caused by space radiation. Although Monte Carlo techniques provide a means to model space radiation using complete, three-dimensional models, reaching a precise solution can require extensive computer resources and long times to perform the calculations. Deterministic codes, such as HZETRN (Ref. 3), are capable of providing faster solutions, but they operate in one dimension and do not incorporate complete physical models. A one-dimensional calculation of space radiation does not account for the three dimensional nature of induced secondary radiation, such as delta-rays, ion fragments, and neutrons. Although they are calculationally more intensive, Monte Carlo codes such as FLUKA (Ref. 4) account for these effects.

The space radiation environment can change rapidly. The speed of this change makes it necessary to have a tool to calculate locations, aspect, and shielding configurations aboard a space craft that provide the maximum possible protection to equipment and personnel. In some scenarios, these calculations need to be performed in a matter of minutes. The straightforward

application of a Monte Carlo code to high energy charged particle transport cannot be performed this quickly using currently available technology.

The goal of this research is to establish a means of gaining the maximum benefit from the accuracy of Monte Carlo calculations while providing a calculation tool that is available quickly enough to allow astronauts to implement a mitigating strategy aboard a spacecraft. To accomplish this goal, lookup tables were created for dose, dose equivalent, and fluence using the most common radiation character and energy of GCR penetrating various depths of likely spacecraft shielding materials and water as a tissue surrogate. The development of these lookup tables will allow Monte Carlo results to be applied to time-sensitive shielding analyses while sacrificing only a minimal amount of accuracy due to the use of a lookup table. It is hoped that this research will directly assist NASA in its challenge of reducing personnel exposure to radiation on a long-term space flight by 20 to 30%.

B. Originality and Justification

The research reported herein consists of three different topics. First, FLUKA lookup tables were developed to support the efforts of NASA-JSC Space Radiation Analysis Group ("SRAG"). SRAG contractor Wyle subcontracted this work to the University of Tennessee because this work had not been previously performed and was necessary to promote SRAG's demand for a high-speed means of analyzing the GCR spectrum with Monte Carlo results. This work is new and original.

To benchmark the efficacy of this lookup tool, the FLUKA lookup tool was utilized to model the Cosmic Ray Telescope for the Effects of Radiation ("CRaTER") telescope. This work

used the dose lookup tables in conjunction with the BO'10 GCR code in order to replicate the measurements made by CRaTER (Ref. 5). Furthermore, a more accurate simulation of the CRaTER telescope was performed in order to judge the efficiency of the lookup table in reproducing the result of a direct simulation. This work represents the first comparison between the FLUKA Monte Carlo Transport code and the experimental data obtained from CRaTER. Therefore, this work is new and original.

Furthermore, this work used the lookup tables and the BO'10 GCR code to create a table of the effective dose to a notional astronaut for a given GCR spectrum, EM shielding, and physical shielding combinations. These tables could be used as a guidepost to examine the impacts of changing the shielding configuration on the effective dose and organ doses to an astronaut behind the shielding.

II. Background

A. Description of the Relevant Dosimetric Quantities

The use of experimental data or a Monte Carlo code to calculate a point quantity can often lead to confusion concerning the meaning of each unit. For example, FLUKA provides a means of calculating dose through its DOSE function (Ref. 4), but FLUKA's DOSE functionality does not calculate absorbed dose, as it is typically conceptualized. Generally, absorbed dose is considered a point quantity. It is the energy absorbed per unit mass of matter at a particular point:

$$D = \frac{d\varepsilon}{dm}$$

Where dε is the energy imparted to the mass, and dm is the infinitesimal mass element (Ref. 6). The energy imparted (ε) is defined as:

$$\varepsilon = \sum T_{in} - \sum T_{out} + \sum Q$$

(Ref. 7) where:

- ΣT_{in} the sum of the kinetic energies of all those directly and indirectly ionizing particles which have entered the volume
- ΣT_{out} the sum of the kinetic energies of all those directly and indirectly ionizing particles which have left the volume
- ΣQ the sum of all the energies released, minus the sum of all energies expended, in any transformations of nuclei and elementary particles which have occurred within the volume

(Ref. 7). When dose is calculated by a Monte Carlo code such as FLUKA, the quantity reported is a cumulative dose across the entire detector region, which is equivalent to:

$$\overline{D} = \frac{1}{m}\int_R D(\vec{r})dm = \frac{1}{m}\int_R \left(\frac{\partial\varepsilon(\vec{r})}{\partial m}\right)dm = \frac{\varepsilon}{m}$$

where D bar represents the cumulative dose in region R, m represents the mass in region R, D(r) is the absorbed dose at point r within R, ε(r) is the imparted energy at point r, and ε is the total energy imparted to R. The cumulative dose provides a good estimation of the absorbed dose in a given region provided that the absorbed dose is not changing rapidly within the region and that the regions are sufficiently small. Therefore, an understanding of the behavior of dose as a function of position in the measurement region and control of the measurement region is essential for developing physically meaningful quantities for comparison with experimental results or with the products of other codes.

This research involved primarily unidirectional radiation, which simplifies the task of normalizing the energy deposition data for comparison with experimental data and other codes. Because the radiation in the simulations is directed axially along a cylinder of material, the variation of the deposited energy changes axially much more rapidly than it does radially. The geometry is symmetric with respect to the angular coordinate, so the absorbed energy is independent of the angular coordinate. Of course, the radiation will not cross the detector entirely in the axial direction. Secondaries will be produced in many different directions, and the primary particle will straggle due to interactions with the target material. However, for radiation that is incident axially, it can be assumed with relatively little loss of accuracy that the radiation travels axially across the length of the detector. Comparison with experimental data is somewhat more straightforward because a detector will detect the deposition of energy within its volume rather than a point quantity such as absorbed dose.

Experimental data that are obtained from instruments such as the CRaTER telescope are typically reported as linear energy transfer ("LET") or lineal energy, rather than dose and dose equivalent (Ref. 8). The ICRU defines LET as:

> The *linear energy transfer* or *restricted linear electronic stopping power*, L_Δ, of a material, for charged particles of a given type and energy, is the quotient of dE_Δ by dl, where dE_Δ is the mean energy lost by the charged particles due to electronic interactions in traversing a distance dl, minus the mean sum of the kinetic energies in excess of Δ of all the electrons released by the charged particles, thus
>
> $$L_\Delta = \frac{dE_\Delta}{dl}$$

(Ref. 9). In other words, the LET accounts for the energy transferred from the incident particle to the medium less the *kinetic energy* of the electrons whose initial kinetic energy exceeds the cutoff energy Δ. Even if the kinetic energy of an electron is subtracted, the electron's binding energy is still included in the calculation. Therefore, even when the cutoff energy is set to zero, the LET (L_0) is generally not equal to 0. Based on the medium of interest, an appropriate cutoff energy can be chosen to obtain an approximation of the energy that is "'locally transferred,'" i.e., that excludes electrons that are so energetic that they exit the medium of interest without depositing a significant amount of their kinetic energy (Ref. 9). The unrestricted LET is the LET in the absence of an energy cutoff and is commonly denoted by L or L_∞. This quantity is equal to the linear electronic stopping power (Ref. 9).

A closely related quantity to LET that is of use in analyzing experimental data is the lineal energy, commonly denoted by y (Ref. 8). The ICRU defines lineal energy as:

> the quotient of ϵ_s by $\bar{l}$, where ϵ_s is the energy imparted to the matter in a given volume by a single energy-deposition event, and $\bar{l}$ is the mean chord length of that volume, thus

$$y = \frac{\in_s}{\bar{l}}$$

(Ref. 9).

As explained above, it is not possible to precisely calculate the microscopic quantity LET using either experimental data or a Monte Carlo code. Monte Carlo codes do not calculate point quantities, and a physical measurement must take place over a finite volume. Rather than LET, the measurements made in CRaTER are more accurately modeled by the concept of lineal energy. While LET represents the instantaneous stopping power at a particular point, lineal energy is the energy imparted in a region divided by the mean path length of radiation through the region:

$$y = \frac{\in}{\bar{x}}$$

where ϵ is the energy imparted, defined above, and x bar is the mean path length through the region (Ref. 10). This quantity is more amenable to calculation by Monte Carlo codes and by physical detectors because Monte Carlo codes and detectors measure and calculate the energy imparted (ϵ) (Ref. 8). However, it is necessary to know the path length of the radiation, which is usually not measured in the physical detector and depends on several factors. Furthermore, the primary particle's incident angle on the detector and the phenomenon of path-length straggling will cause further variation in the particle's path length through the detector (Ref. 8). The path length can be estimated using a number of techniques. For example, for their analysis of the CRaTER telescope, Case *et al*. used a Monte Carlo simulation of particles whose initial trajectories would allowed them to meet the established detector coincidence criteria (Ref. 8).

This analysis resulted in a calculated path length that was one percent longer than the detector thickness (Ref. 8). Given this small variation, it is likely that the detector thickness can be used in most instances.

Measurements of absorbed dose are extremely useful as measurements of the energy absorbed in a volume; however, it has long been recognized that the impact of the absorbed energy on biological organisms differs based on the character and energy of the radiation. In other words, some forms of radiation cause more damage to tissue than others. The calculation of the quantities dose-equivalent, equivalent dose, and effective dose accounts for these differences by assigning a quality factor to be multiplied to the absorbed dose in order to obtain a quantity that better represents the impact of the radiation on living tissue (Ref. 10).

Equivalent dose is the product of the absorbed dose and a weighting factor which depends on the identity of the radiation. The particles are assigned different factors based on a table (Ref. 11, 12). For example, gamma rays are assigned a weighting factor of 1, and alphas and other heavy ions are assigned a factor of 20. Therefore, for a heavy ion, the equivalent dose is equal to the twenty times the absorbed dose. Although the use of these factors may be sufficient in other applications, equivalent dose is not well-suited to space radiation. Space radiation contains a plethora of heavy ion species, and the use of a single factor for all heavy ions will not account for the different biological impact of higher-energy ions with lower LET compared to high-LET ions which come to a stop in the body. As a result, for space radiation, the NCRP has endorsed the use of organ dose-equivalent over equivalent dose (Ref. 13).

Dose-equivalent is defined in a matter analogous to the definition of equivalent dose. The dose-equivalent is the absorbed dose multiplied by a quality factor, which is derived from the LET of the particle:

$$H = QD$$

(Ref. 10). The recommended quality factors have evolved over time. Prior to 1990, the quality factors were those shown in Table 1 (Ref. 10, 14). However, in 1990, ICRP Publication 60 updated the quality factors to those shown in Table 2. The calculations presented in this work follow the quality factors recommended in ICRP 60 (Ref. 12), and these are the quality factors used unless otherwise noted.

In addition to taking into account the differences in the energy absorbed from radiation at the cellular level, effective dose accounts for the different impact to human life of the absorption of energy by organs in the human body. This calculation recognizes that some organs are more sensitive to radiation than others and that therefore the biological impact of radiation to those organs will result in more harm than radiation to other, less sensitive organs. Effective dose is generally defined as the summation of the equivalent dose to each organ multiplied by a tissue weighting factor:

$$E = \sum_T w_T H_T$$

where T represents the organs to be considered, w_T represents the tissue weighting factor, and H_T represents the equivalent dose. The tissue weighting factors approved by the NCRP and ICRP than the organ equivalent dose be used for the purposes of calculating the effective dose for

Table 1: ICRP 26 Quality Factors (Ref. 14)

LET (keV μm^{-1})	Q
3.5 or less	1
3.5-7.0	1-2
7.0-23	2-5
23-53	5-10
53-175	10-20
Gammas, x-rays, electrons, positrons (any LET)	1

Table 2: ICRP 60 Quality Factors (Ref. 12)

LET, L (keV μm^{-1})	Q
<10	1
10-100	0.32L-2.2
>100	$300/\sqrt{L}$

Table 3: Standard tissue weighting factors used in effective dose calculations (Ref. 10).

Tissue	w_T
Gonads	0.20
Bone Marrow (Red)	0.12
Colon	0.12
Lung	0.12
Stomach	0.12
Bladder	0.05
Breast	0.05
Liver	0.05
Esophagus	0.05
Thyroid	0.05
Skin	0.01
Bone Surface	0.01
Remainder	0.05

space flight both within and outside of LEO (Ref. 13). In accordance with this recommendation, this work will use the effective dose equivalent, calculated using dose-equivalent rather than equivalent dose.

B. Space Radiation Transport Codes

1. Description of the Relevant Codes

FLUKA Monte Carlo Transport Code is "general purpose tool for calculations of particle transport and interactions with matter, covering an extended range of applications spanning from proton and electron accelerator shielding to target design, calorimetry, activation, dosimetry, detector design, Accelerator Driven Systems, cosmic rays, neutrino physics, radiotherapy etc." (Ref. 4). Generally, FLUKA transports charged particles using a Multiple Coulomb scattering model developed for FLUKA by Ferrari *et al.* (Refs. 15 and 16). Additional description of the features of FLUKA that were enabled for the calculations performed in this work appears below. A summary of the physical models included in FLUKA can be found in Reference 4. Some of the notable features for the purposes of this investigation include FLUKA's treatment of charged particle energy loss. FLUKA has the ability to transport delta-rays and incorporates additional lower-order effects to the Bethe-Bloch formula such as the Barkas Z^3 effect, the Bloch Z^4 effect, etc. (Ref. 4).

HETC-HEDS is a Monte Carlo transport code designed by Townsend *et al.* specifically for the transport of space radiation (Ref. 17). HETC-HEDS is an extension of the previously-existing HETC code, which transported only protons, neutrons, pions, and muons. HETC used

the continuous slowing down approximation which incorporates the Bethe-Bloch stopping power formula to calculate the energy loss of transported charged particles. The model also incorporated calculations for multiple Coulomb scattering, pion decay and capture, muon decay, elastic neutron collisions, and inelastic collisions with hydrogen. Townsend *et al.* developed HETC-HEDS in 2005 as an extension to HETC. HETC-HEDS added a heavy ion transport capability which accounted for nucleus-nucleus interactions and incorporated a model for fragmentation and spallation. Total reaction cross sections for heavy ions were formulated using the model developed by Tripathi *et al.* (Ref. 18). Total cross sections were then calculated by multiplying the total reaction cross section as developed by Tripathi by the ratio of total to reaction cross sections, calculated using the optical potential model that was developed by NASA Langley (Refs. 19 and 20). Notably, HETC-HEDS does not account for delta ray production (Ref. 21).

HZETRN is a deterministic transport code which numerically solves the Boltzmann transport equation in one dimension (Ref. 22). HZETRN solves the Boltzmann equation using the straight-ahead and continuous slowing down approximations. The Boltzmann transport equation, incorporating the straight-ahead and continuous slowing down approximations, is expressed as follows (Ref. 23):

$$\bar{B}\left[\varphi_j(x,E)\right] = \sum_k \int_E^\infty \sigma_{jk}(E,E')\varphi_k(x,E')dE'$$

The operator $\bar{B}$ is expressed as (Ref. 23):

$$\bar{B}\left[\varphi_j(x,E)\right] = \left[\frac{\partial}{\partial x} - \frac{1}{A_j}\frac{\partial}{\partial E}S_j(E) + \sigma_j(E)\right]\varphi_j(x,E')$$

In the above equations, $\varphi_i(x,E)$ represents the flux of particle i at kinetic energy per nucleon E and depth x, A_i is the atomic mass of particle i, and $S_i(E)$ is the stopping power of particle i with kinetic energy per nucleon E. The macroscopic cross section $\sigma_i(E)$ is the total cross section for particle i at kinetic energy per nucleon E, and $\sigma_{ih}(E,E')$ is the macroscopic differential cross section covering interactions where particle h is traveling at kinetic energy per nucleon E' and the interaction produces particle i travelling at kinetic energy per nucleon E (Ref. 23). HZETRN produces a numerical solution to this equation for given input parameters.

2. Existing Comparisons of HZETRN, HETC-HEDS, and FLUKA

Previous work has shown good agreement between HZETRN, HETC-HEDS, and FLUKA. Heinbockel *et al.* published two separate papers in 2011 comparing the performance of these three codes for both SPE and GCR spectra in slab calculations similar to the calculations performed for this work (Refs. 22 and 25). In these papers, Heinbockel compared the performance of the codes for dose and dose equivalent calculations but also incorporated a fluence comparison.

Heinbockel's comparison of these three codes for both GCR and SPE spectra compared results created using a 20 g cm^{-2} aluminum shield with a 30 g cm^{-2} water target behind it. For the SPE comparison, Heinbockel used a spectrum created by Webber to model the February 1956 SPE (Ref. 22). For the GCR comparison, Heinbockel used the spectrum for the 1977 solar minimum calculated using Badwhar and O'Neill's model (Ref. 26). With respect to both the SPE and GCR spectra, Heinbockel noted several areas where the codes did not agree well,

particularly in fluence calculations. For example, when comparing the resulting heavy ions on breakup of an incident carbon beam, FLUKA calculated significantly lower values for the production of heavier ions such as boron and beryllium than HZETRN and HETC-HEDS. Heinbockel noted that differences in energy deposition calculations between the three codes likely result from differences in calculation methodology, differences in cross section library, and, with respect to dose equivalent, differences in the quality factors (Ref. 25).

The three codes exhibit substantial differences in their calculation of dose. FLUKA tallies dose by recording all energy deposited by any transported particle in a given region. The sum of the deposited energy is then divided by mass to give a cumulative dose. The HETC-HEDS calculation of dose looks instead at the difference in the particle's energy between its entry into and exit from the region of interest. HETC-HEDS handles low energy neutrons (less than a preselected cutoff, usually 20 MeV) differently, performing a calculation based on the neutron flux and KERMA factors. HZETRN calculates dose by integrating the calculated fluence with the stopping power of the ion being transported. However, unlike HETC-HEDS and FLUKA, the version of HZETRN used for the simulations referenced in this work does not transport some particles, such as muons, pions, electrons, positrons, and photons. Under some circumstances, these particles can contribute substantially to deposited energy (Ref. 25). Furthermore, of the three codes, only FLUKA transports delta-rays.

The codes also differ in their calculations of dose equivalent. Most importantly, HETC-HEDS uses the ICRP-26 quality factors (Ref. 14) rather than the ICRP-60 quality factors (Ref. 12). Not surprisingly, for GCR spectra, FLUKA and HZETRN showed better agreement than

the codes showed with HETC-HEDS. The ICRP-26 and ICRP-60 quality factors differ substantially from one another and should be expected to provide disparate results.

III. Lookup Table Calculations

A. Description of the Calculations

This work will undertake the development of lookup tables and parameterizations for energy deposition and fluence data in water for several heavy ions of typical GCR energy after the particles penetrate varying layers of typical shielding materials from space applications using FLUKA Monte Carlo Transport Code. The particles examined include the most common isotopes of heavy ions ranging from protons (Z=1) to iron ions (Z=26). Energies range from 1 MeV/n to 10 GeV/n as follows: 1, 5, 10, 20, 40, 60, 80, 100, 200, 400, 600, 800, 1000, 1500, 2000, 2500, 3500, 5000, 10000 MeV/n. The ions are generated in free space and penetrate varying thickness of aluminum and polyethylene shielding prior to entering 100 g cm^{-2} of water, where the fluence and energy deposition measurements are made. The shielding depths are 0, 0.0016, 0.0025, 0.004, 0.0063, 0.01, 0.016, 0.025, 0.04, 0.063, 0.1, 0.16, 0.25, 0.4, 0.63, 1, 1.6, 2.5, 4, 6.3, 10, 16, 25, 40, 63, and 100 g cm^{-2}. These shielding depths represent the thickness of the individual shielding layers. In other words, the shield consists of a layer of aluminum at one of these shielding depths followed by a layer of polyethylene at one of these depths. Measurements of the desired quantities (particle fluences, dose, dose equivalent) are made at the same depths in the water layer. These energies and shielding combinations were used because they were the combinations that were requested by NASA-Johnson Space Center SRAG for this work (Ref. 29). SRAG intends to use this lookup tool initially for the analysis of radiation associated with the International Space Station.

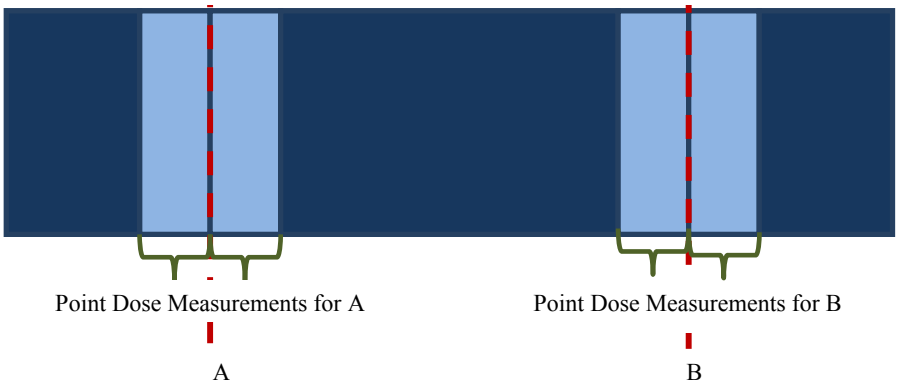

Figure 1: Two detectors, A and B, showing the small slivers used to calculate dose and dose equivalent (Ref. 30).

For each detector location, dose and dose equivalent were calculated in a small sliver (0.0001 g cm^{-2}) both before and after the detector location. The arrangement of these detectors is shown in Figure 1. The use of a small detector both before and after the desired detector location serves three purposes. First, although dose is by definition a point quantity, Monte Carlo codes such as FLUKA are not capable of calculating point quantities. Therefore, a FLUKA dose calculation is in reality a cumulative dose over a defined region. This phenomenon requires that the detector have a finite thickness. These simulations used 0.0001 g cm^{-2} as a thickness that was small in relation to detector separation (a minimum of 0.0016 g cm^{-2}) but is large enough to avoid high variability and erratic calculations due to infrequent events occurring near detector boundaries. Second, the use of two detectors provides a means of predicting the rate of change of the quantities, which will provide for easier parameterization when peak energy deposition occurs between two boundaries. Third, the use of two close detectors provides a means of estimating stopping power (-dE/dx) by comparing the difference in energy deposition between the two detectors. When the fluence data is incorporated, a rough approximation of LET can be obtained.

It should be noted that the scoring for the detector that is nominally located at 0 g cm^{-2} of water was calculated such that the first detector spanned from 0 to 0.0001 g cm^{-2} and that the second detector spanned from 0.0001 to 0.0002 g cm^{-2}. Therefore, although this proposal refers to this point as 0 g cm^{-2}, it is more accurately located at 0.0001 g cm^{-2}, and this value is used to enable the development of figures using the logarithm of depth. The detectors at 100 g cm^{-2} use the opposite approach. The first detector spans from 99.9999 to 100 g cm^{-2}, and the second detector spans from 100 to 100.0001 g cm^{-2}. Therefore, the water column is actually slightly larger than 100 g cm^{-2}, but the detector is centered at 100 g cm^{-2}. This approach was adopted because it is not possible to calculate the dose at 0 g cm^{-2} because it is located on the shielding boundary, so calculating the dose at 0 g cm^{-2} precisely would be a fiction. Furthermore, the addition of 0.0001 g cm^{-2} to the back of the water column will have negligible, if any, impact to the calculated data quantities.

The dose calculations were performed in the spatial mesh described above using FLUKA's binning detector USRBIN. FLUKA's DOSE scoring particle was used to obtain the dose information (Ref. 4). As configured, this detector calculates the deposited energy, and the calculation of energy per unit mass was performed using a post-processing tool that was developed.

The dose equivalent calculation was performed with USRBIN using the same mesh, but the quantity DOSEQLET was scored. DOSEQLET calculates dose equivalent using the ICRP-60 Q(LET) calculation (Refs. 4 and 12). It is noted that FLUKA incorporates other methods for calculating dose equivalent that may be appropriate under other circumstances.

Fluence data was gathered using the parameters requested by SRAG (Ref. 31). Inverse cosine weighted one-way (forward) fluence was recorded. For each detector in water, FLUKA's boundary fluence detector USRBDX was used to calculate fluence data. For each detector, forward fluence data was recorded for heavy ions from protons (Z=1) to the particle with the same identity as the source particle. For example, for incoming lithium particles, fluence data was recorded for particles with Z=1, Z=2, and Z=3. It is important to note that the fluence detectors record the fluence from all isotopes within the given atomic number. This arrangement contrasts with the creation of the source particles, which are entirely of the most common isotope.

For each particle, the fluence was recorded in twenty energy bins, which were spaced logarithmically from 1 MeV/n to 10 GeV/n. That is, the first bin recorded particles between 1 and 1.58 MeV, and so on. The fluence was further subdivided into ten solid angles. Because only forward fluence was recorded, the bins were divided into ten linearly equal bins covering solid angles (Ω) from 0 to 2π. The bins were spaced from 0-0.2π, 0.2π-0.4π, etc.

An enormous number of calculations were required to obtain data for all parameters requested by SRAG. Simulations were conducted for 26 particles at 19 different energies through 676 different shielding combinations, for a total of 333,944 simulations. From each simulation, 52 dose data and 52 dose equivalent data were calculated, for a total of 34,730,176 energy deposition values. At each of the 26 detectors, 200 fluence data were recorded for each particle with Z less than the incoming particle, yielding 93,771,475,200 data. Of course, many

of the fluence data were zero because they recorded fluence for energies above that of the incoming particle, which were not possible for the energy ranges involved.

The calculations were performed on the Newton High Performance Computer Cluster, operated by the University of Tennessee at Knoxville (Ref. 32). Each of the 333,944 simulations was run a minimum of five times. Each run concluded when the transport of 10,000 primary particles was completed or after the simulation had been running for 90 minutes. Although the Newton Cluster's short time limitation is two hours, it was necessary to reserve a substantial amount of time to ensure that the output files could be written and that FLUKA and the script used to submit the jobs could reach completion prior to timeout. Below 400 MeV/n, all primary particles were run in the vast majority of cases, resulting in 50,000 histories for each simulation (5 runs with 10,000 histories). For 10 GeV/n iron ions penetrating the thickest shield, as few as 100 primary particles were calculated in some simulations. Compared to the lower energies, many more runs were required to obtain acceptable statistics.

B. FLUKA Physics Settings

FLUKA Version 2011.2 was used to complete these calculations. As stated above, FLUKA can accurately model space radiation over a wide range of particle identities and energies, so FLUKA is an excellent choice for modeling GCR spectra, which consist of a wide energy spectrum. Although FLUKA does not present interchangeable physical models except under specific circumstances, FLUKA provides a wide range of control over parameters such as delta ray transport, energy thresholds, and which particles are transported and analyzed.

The FLUKA User's Manual (Ref. 4) recommends the use of DPMJET-II.5 for cosmic ray applications, and this option was used for these simulations per the request of SRAG. SRAG requested that these simulations be run using FLUKA's PRECISIOn defaults. The PRECISIOn defaults are activated using the DEFAULTS card (Ref. 4). The FLUKA User's Manual (Ref. 4) lists the enabled transport phenomenon for the PRECISIOn defaults as follows:

- EMF on
- Rayleigh scattering and inelastic form factor corrections to Compton scattering and Compton profiles activated
- Detailed photoelectric edge treatment and fluorescence photons activated
- Low energy neutron transport on down to thermal energies included, (high energy neutron threshold at 20 MeV)
- Fully analogue absorption for low-energy neutrons
- Particle transport threshold set at 100 keV, except neutrons (1E-5 eV), and (anti)neutrinos (0, but they are discarded by default anyway)
- Multiple scattering threshold at minimum allowed energy, for both primary and secondary charged particles
- Delta ray production on with threshold 100 keV (see option DELTARAY)
- Restricted ionisation fluctuations on, for both hadrons/muons and EM particles (see option IONFLUCT)
- Tabulation ratio for hadron/muon dp/dx set at 1.04, fraction of the kinetic energy to be lost in a step set at 0.05, number of dp/dx tabulation points set at 80 (see options DELTARAY, EMFFIX, FLUKAFIX)
- Heavy particle e+/e- pair production activated with full explicit production (with the minimum threshold = 2m_e)
- Heavy particle bremsstrahlung activated with explicit photon production above 300 keV
- Muon photonuclear interactions activated with explicit generation of secondaries
- Heavy fragment transport activated

These simulations used a particle transport threshold of 100 keV/n for all particles other than neutrons. This transport threshold is the default for the precision defaults option selected by SRAG. For particles that were not stopped at higher energies through interactions, FLUKA

ceased particle transport when the energy of the ion was slowed down to 100 keV/n. From this point, FLUKA approximates the range of the particle, and the particle's energy is deposited uniformly along the path from its location to the end of its range. Although FLUKA accounts for magnetic fields in calculating these paths, no magnetic fields were used in this simulation, so the path is simply a straight line from the particle's location when it slows to 100 keV/n to the end of its range. If the particle crosses a material boundary, the range is recalculated for the new material.

Using option THRESHOLd, the user can set the minimum energy at which FLUKA will calculate the effects of hadron elastic and inelastic collisions as well as for star scoring. By default, FLUKA sets these thresholds to the transport thresholds for elastic and inelastic collisions, at 20 MeV for proton and neutron stars, and at 50 MeV for all other stars. These simulations used a threshold of 100 keV/n for elastic and inelastic hadron collisions and for star transport.

FLUKA allows the user to turn on and adjust delta ray production for charged hadrons and muons using the DELTARAY option. For these calculations, the DELTARAY option was activated using FLUKA's default settings for all materials used in the simulation. The production of discrete delta rays was enabled above 100 keV/n. FLUKA treats energy loss below this threshold as occurring continuously. It should be noted that this setting has no impact on delta rays produced by electrons and positrons, which are calculated and transported regardless of the DELTARAY option (Ref. 4).

FLUKA's PAIRBREM card provides the user a means to toggle the energy thresholds for pair production and for bremsstrahlung. When PAIRBREM is enabled, FLUKA will simulate pair production and bremsstrahlung for hadrons and light ions (alphas and lighter). Under the options used for these simulations, pair production was enabled for all particles being transported. Although FLUKA's default for the high precision defaults is to cut off bremsstrahlung calculations at 300 keV/n, the options used in these simulations provided for bremsstrahlung reactions to occur at any energy above the transport threshold of 100 keV/n. As with the other options, these selections were effective for all materials used in this simulation (Ref. 4).

FLUKA provides the user great flexibility in selecting the methods by which FLUKA will calculate energy losses for charged particles. As discussed above, below the transport threshold, which was set for 100 keV/n for these simulations, FLUKA simply projects the range of the ion and distributes the remaining kinetic energy uniformly along its track. Above the threshold, the user has the option of enabling delta ray production and to simulate ionization fluctuations. FLUKA simulates ionization fluctuations according a statistical model created by Fasso (Ref. 33), rather than the commonly used models proposed by Landau and Vavilov. The user can choose between restricted and unrestricted energy loss fluctuations with two different settings allowed for hadrons/muons and electrons/positrons. If neither delta ray nor ionization fluctuations are enabled, transport proceeds according to the continuous slowing down approximation (Ref. 4). These simulations specified restricted energy loss fluctuations for both

hadrons/muons and electrons/positrons and allowed delta ray production for the entire range of transport energies, down to 100 keV/n.

C. FLUKA Geometry

As described above, the geometry for this problem was entered into FLUKA as a right circular cylinder of radius 10^5 cm, which is arbitrarily large for these simulations. This cylinder was surrounded on the lateral sides by BLKHOLE, which terminates the calculation of particle transport. The interface between the water target and the shielding materials (aluminum, polyethylene, or vacuum in the unshielded case) was placed at z=0 cm. The water target extended from z=0 cm to z=100.0001 cm. As discussed above, 0.0001 cm was added to the target to allow for the placement of mirror image energy deposition detectors at z=100 cm. Behind the water target is a vacuum, followed by BLKHOLE.

From z=0 cm, the length of shielding material was calculated using the shielding thicknesses specified by SRAG and densities of 2.699 and 0.964 g cm^{-2} for aluminum and polyethylene respectively. A vacuum region was placed prior to the shield with BLKHOLE thereafter. Particles were generated in the vacuum on the xy axis at z=-150 cm and pointed at the origin.

D. FLUKA Materials Settings

These simulations involve three materials in which energy is deposited—aluminum, polyethylene, and water. FLUKA's preprogrammed aluminum material, ALUMINUM (material

number 10) was used for the aluminum shield. MATERIAL and COMPOUND cards were used to define the water and polyethylene from their elements. Water was defined as a compound consisting of 2 HYDROGEN (material number 3) atoms and one OXYGEN (material number 8) atom, with a density of 1 g cm^{-3}. Polyethylene was defined as a compound consisting of two HYDROGEN atoms and one CARBON (material number 6) atom with a density of 0.964 g cm^{-3}.

Per the FLUKA User's Manual, ALUMINUM is programmed with an atomic number of 13, an atomic mass of 26.981538 amu, and a density of 2.699 g cm^{-3}. HYDROGEN is programmed with an atomic number of 1, an atomic mass of 1.00794 amu, and a density of 0.0000837 g cm^{-3}. FLUKA's CARBON is programmed with an atomic number of 6, an atomic mass of 12.0107 amu, and a density of 2.000 g cm^{-3}.

The simulations also incorporated the materials BLKHOLE (material number 1) and VACUUM (material number 2). These materials are both voids. BLKHOLE terminates the track of any particle that touches it. In contrast, VACUUM does not terminate the particle's track.

E. FLUKA Scoring

To obtain the dose, dose equivalent, and fluence calculations discussed above, FLUKA's USRBIN and USRBDX scoring cards were used. The USRBIN card provides a simple means of scoring the energy deposition in a defined volume using the DOSE scoring particle (Ref. 4). As described in more detail above, the scoring regions were comprised of cylindrical slivers that

were 0.0001 g cm^{-2} thick. Two slivers were placed symmetrically at each scoring depth with the exception of 0 g cm^{-2}, where they were shifted into the water column. The result of this calculation is a cumulative dose, which is averaged over the entire mass of the scoring region. Because the scoring region is arbitrarily large, it was necessary to multiply the cumulative dose by the area of the detector ($\pi*10^{10}$ cm^2) to obtain a cumulative dose in units of Gy*cm^2, which is equivalent to energy deposited divided by the areal density. This parameter produces results that are comparable between detectors that do not share the same size. Because most of the energy is deposited near the cylinder's axis and the cylinder is arbitrarily large, omitting this correction would make the dose dependent on the selected cross sectional area of the cylinder, which is not a physically meaningful parameter for these simulations. Furthermore, some subsequent calculations used detectors of varying sizes, so recording the energy divided by the areal density in units of Gy*cm^2 allows for ready comparison among these detectors.

Dose equivalent was calculated using a set of scoring cards that were identical to the USRBIN cards described above except that they recorded DOSEQLET events instead of DOSE. DOSEQLET calculates the dose equivalent using the ICRP-60 quality factors and unrestricted LET (Ref. 4).

Fluences were recorded using FLUKA's USRBDX scoring card. USRBDX detects the fluence crossing a boundary, which in this case was defined to be the intersection of the plane at the measurement depths requested at SRAG and the target. The USRBDX cards were set up to use one-way fluence scoring that is inverse cosine-weighted, binned linearly into 10 angular bins and logarithmically into 20 energy bins. Because only the forward fluence is measured, the

angular bins span solid angles from 0 to 2π sr in increments of 0.2π. The energy bins run from 1 MeV/n to 10 GeV/n in 20 logarithmic steps. In other words, the first bin runs from 1 to $1*10{,}000^{.05}$ MeV/n, the second bin runs from $1*10{,}000^{.05}$ to $1*10{,}000^{.10}$ MeV/n, etc. For the sake of consistency, the same binning structure was used for all incident particle energies. Therefore, FLUKA calculated the 10 GeV/n fluence for 1 MeV/n as well as 10 GeV/n incident protons. The results of each fluence scoring card are recorded as the double differential fluence (particles cm^{-2} GeV^{-1} sr^{-1}).

These simulations scored fluence for particles ranging from protons to the particles of the same atomic number as the incident particles. In other words, only protons were scored for incident protons, protons and alphas were scored for incident alphas, etc. The USRBDX card allows the user to score the fluences of specific particles or family of particles using FLUKA's particle codes or the AUXSCORE card. For these simulations, proton and alpha fluences were recorded using the pre-defined PROTON and 4-HELIUM particles without the use of AUXSCORE. Particles heavier than alpha particles were scored by recording all HEAVYIONs with the USRBDX card and then applying AUXSCORE to obtain particles with only the requisite atomic number.

IV. Characteristics of FLUKA Lookup Table Results

The development of the FLUKA tool required significant processor time and required the storage of significant amounts of data. Simulations were run for every combination of 26 incident particles at 19 initial energies through 26 different layers of aluminum and 26 different layers of polyethylene. Altogether, these combinations result in 333,944 distinct simulations, each of which was run a minimum of five times. Many of the simulations were run more than five times in order to obtain acceptable statistics. Each simulation recorded dose and dose equivalent both before and after each of the 26 detector depths, requiring the storage of 34,734,176 energy deposition data points. The fluence tables resulted in the storage of even more data. For each incident particle, the fluence of the particles with lower atomic number than the incident particles were recorded at ten different solid angles and twenty different energies. Therefore, the fluence data across one detector for an incident iron ion would generate 5,200 data points. Overall, the lookup tool recorded 23,442,868,800 fluence data points. The unprocessed output files produced to generate the lookup tool occupied approximately 500 gigabytes on the Newton Cluster. Because of the extreme number of data generated, it is not practical to reproduce the data tables in their entirety in this work. Initial review of the FLUKA lookup tables showed that the results were consistent with available data from sources such as SRIM (Ref. 34). Both SRAG and UT have complete sets of the data. A sample of the data for one ion, initial energy, aluminum thickness, and polyethylene thickness is provided below. 400 MeV/n oxygen ions and 0.004 g cm^{-2} of aluminum followed by 0.0063 g cm^{-2} of polyethylene were

arbitrarily selected for the purpose of providing an example. The energy deposition data for this configuration is available in Table 4, and a summary of the fluence data can be found in Table 5.

Figure 2 shows a plot of absorbed dose in water as a function of water depth for incident 400 MeV/n oxygen ions. In this case, the water target was shielded by 0.004 g cm^{-2} of aluminum followed by 0.0063 g cm^{-2} of polyethylene. The plot resembles the typical depth-dose profile, with relatively flat dose deposition at the beginning of the trajectory and then a peak near the end of its range, where the most energy is deposited consistent with the Bethe-Bloch equation. However, at the end of the incident particle's range, the dose does not decrease immediately to 0 mGy. There is a tail that results from the secondary particles produced from fragmentation, bremsstrahlung, and ionizations near the end of the range. Therefore, even though the incident particle has reached the end of its range, it may produce electrons and secondary ions that deposit energy significantly deeper in the target. Based on the large number of points that SRAG requested at the beginning of the water target, it appears from this graph that there is significant variation at the shallowest depths. However, an examination of this same plot on the logarithmic scale, shown in Figure 3, shows that the variation at these depths is not as significant as it appears in the linear plot in Figure 2. For this plot, the point that is plotted at 0 g cm^{-2} in the linear version is plotted at 0.0001 g cm^{-2} (at the end of the detector rather than the beginning of the detector). This change allows this point to be plotted on the logarithmic plot without meaningfully changing the underlying data. Figure 3 shows that the absorbed dose seems to dip slightly following the detector at 0 g cm^{-2} and remain relatively constant until 10 g cm^{-2}, where it increases sharply to the peak located at 16 g cm^{-2}. The absorbed dose drops sharply, lowering by

Table 4: Energy Deposition Data for 400 MeV/n ^{16}O ions with 0.004 g cm^{-2} Aluminum Shield and 0.0063 g cm^{-2} Polyethylene Shield.

H_2O Depth (g/cm^2)	Dose1 (mGy)	Error (%)	Dose2 (mGy)	Error (%)	DoseEq1 (mSv)	Error (%)	DoseEq2 (mSv)	Error (%)
0	0.32	0.3	0.29	0.2	1.17	0.7	1.14	1.1
0.0016	0.30	0.1	0.31	0.4	1.14	0.4	1.16	1.4
0.0025	0.30	0.2	0.31	0.1	1.14	0.3	1.14	0.3
0.004	0.30	0.3	0.31	0.3	1.14	0.3	1.15	0.3
0.0063	0.31	0.2	0.32	0.4	1.14	0.1	1.15	0.1
0.01	0.31	0.2	0.32	0.3	1.16	0.5	1.16	0.5
0.016	0.31	0.2	0.32	0.4	1.16	0.4	1.17	0.4
0.025	0.32	0.2	0.32	0.3	1.16	0.4	1.17	0.5
0.04	0.32	0.3	0.33	0.3	1.16	0.3	1.17	0.4
0.063	0.32	0.2	0.33	0.4	1.16	0.2	1.18	0.3
0.1	0.33	0.2	0.34	0.4	1.17	0.5	1.18	0.3
0.16	0.33	0.2	0.34	0.6	1.17	0.3	1.18	0.3
0.25	0.33	0.3	0.34	0.4	1.17	0.3	1.18	0.3
0.4	0.33	0.2	0.35	0.3	1.17	0.2	1.18	0.2
0.63	0.33	0.3	0.34	0.4	1.17	0.2	1.19	0.3
1	0.33	0.5	0.35	1.0	1.20	2.0	1.24	3.2
1.6	0.33	0.3	0.34	0.2	1.19	0.5	1.20	0.4
2.5	0.33	0.4	0.34	0.2	1.19	0.3	1.20	0.2
4	0.33	0.6	0.34	0.3	1.21	0.5	1.22	0.4
6.3	0.32	0.4	0.34	0.3	1.26	0.5	1.27	0.5
10	0.33	0.4	0.34	0.6	1.44	2.4	1.44	1.6
16	0.37	0.3	0.39	0.4	2.32	0.4	2.35	0.7
25	0.08	0.7	0.08	1.0	0.39	5.8	0.37	3.3
40	0.03	1.8	0.04	15.7	0.06	17.7	0.19	67.8
63	0.02	3.2	0.02	6.3	0.06	21.9	0.07	23.4
100	0.00	4.2	0.00	4.1	0.01	21.7	0.01	23.7

Table 5: Summarized Fluence Data for 400 MeV/n ^{16}O ions with 0.004 g cm^{-2} Aluminum Shield and 0.0063 g cm^{-2} Polyethylene Shield.

Water Depth (g/cm^2)	Fluence by Ion Identity (#/primary)							
	Z=1	Z=2	Z=3	Z=4	Z=5	Z=6	Z=7	Z=8
0.0000	0.005	0.001	0.000	0.000	0.000	0.000	0.000	0.999
0.0016	0.005	0.001	0.000	0.000	0.000	0.000	0.000	0.999
0.0025	0.006	0.001	0.000	0.000	0.000	0.000	0.000	0.999
0.0040	0.005	0.001	0.000	0.000	0.000	0.000	0.000	0.999
0.0063	0.007	0.001	0.000	0.000	0.000	0.000	0.000	0.999
0.010	0.007	0.001	0.000	0.000	0.000	0.000	0.000	0.999
0.016	0.010	0.001	0.000	0.000	0.000	0.000	0.000	0.999
0.025	0.015	0.002	0.000	0.000	0.000	0.000	0.000	0.998
0.040	0.023	0.002	0.000	0.000	0.000	0.000	0.000	0.997
0.063	0.031	0.003	0.000	0.000	0.000	0.001	0.001	0.996
0.10	0.040	0.004	0.000	0.000	0.000	0.001	0.001	0.995
0.16	0.064	0.006	0.001	0.000	0.001	0.001	0.002	0.992
0.25	0.087	0.009	0.001	0.001	0.001	0.002	0.002	0.987
0.40	0.135	0.013	0.002	0.001	0.001	0.003	0.004	0.980
0.63	0.190	0.021	0.002	0.001	0.002	0.005	0.006	0.970
1.0	0.285	0.033	0.004	0.002	0.003	0.007	0.009	0.953
1.6	0.421	0.050	0.006	0.003	0.004	0.011	0.014	0.927
2.5	0.615	0.077	0.009	0.005	0.007	0.016	0.021	0.889
4.0	0.891	0.116	0.014	0.007	0.011	0.025	0.032	0.831
6.3	1.251	0.172	0.020	0.010	0.015	0.036	0.045	0.750
10	1.748	0.257	0.028	0.015	0.022	0.052	0.059	0.632
16	2.210	0.364	0.038	0.020	0.030	0.067	0.071	0.481
25	1.848	0.382	0.035	0.014	0.017	0.016	0.001	0.000
40	1.160	0.190	0.010	0.001	0.000	0.000	0.000	0.000
63	0.534	0.046	0.000	0.000	0.000	0.000	0.000	0.000
100	0.184	0.000	0.000	0.000	0.000	0.000	0.000	0.000

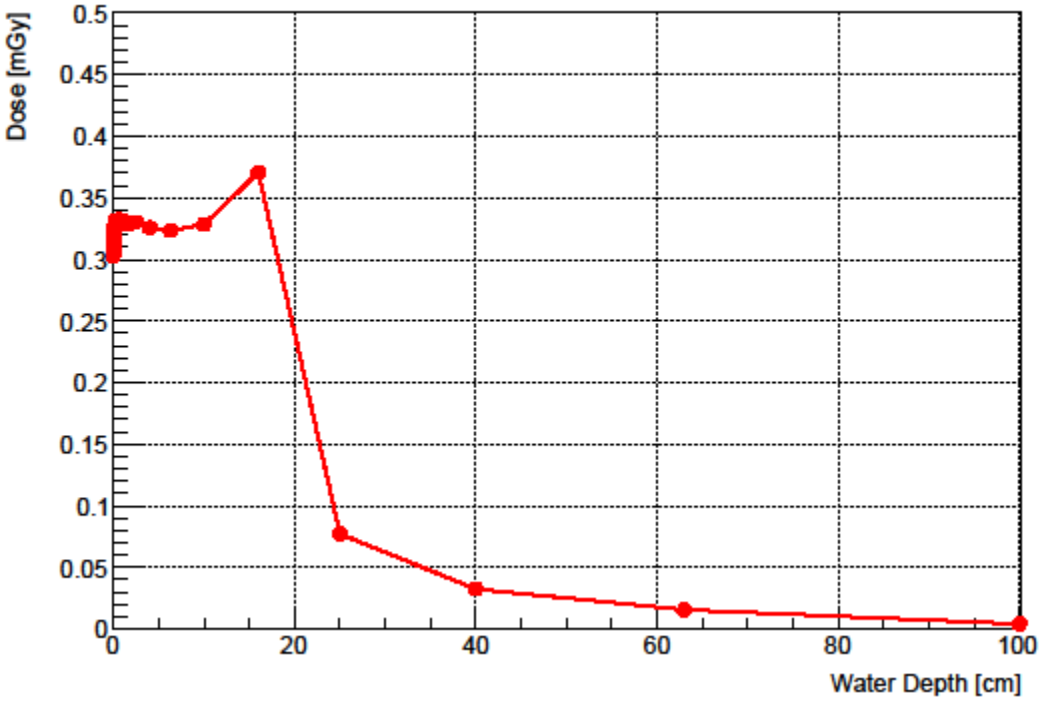

Figure 2: Depth-Dose Curve for Water Target behind 0.004 g cm^{-2} Al and 0.0063 g cm^{-2} Poly in Linear Scale

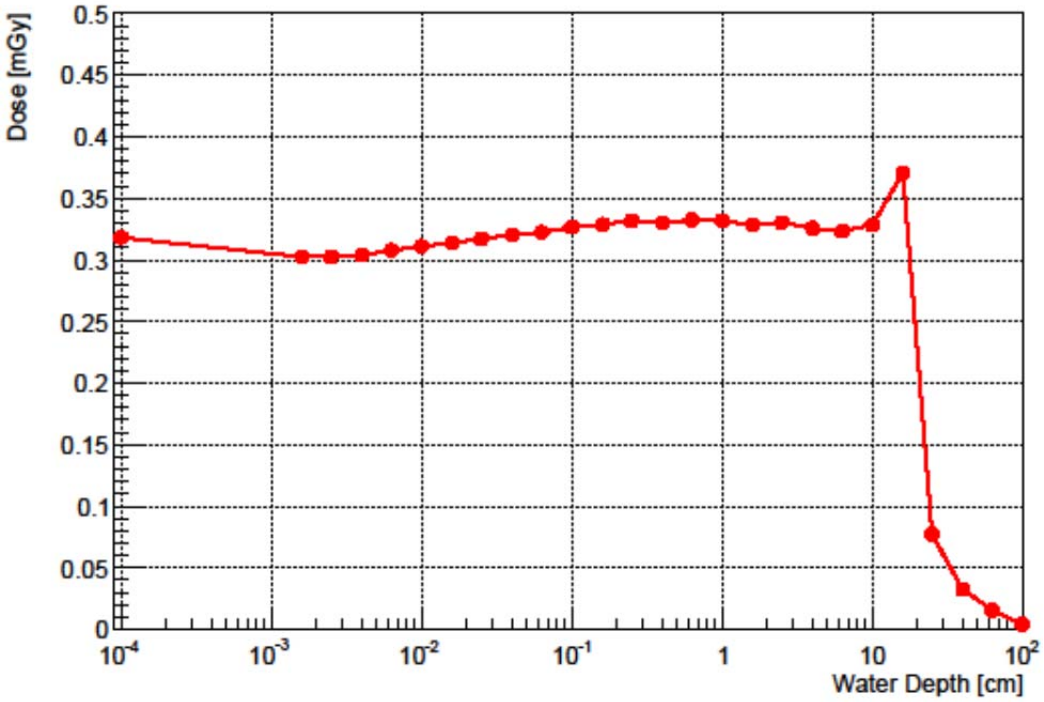

Figure 3: Depth-Dose Curve for Water Target behind 0.004 g cm^{-2} Al and 0.0063 g cm^{-2} Poly in Logarithmic Scale

approximately a factor of five between 16 and 25 g cm^{-2}. Beyond 25 g cm^{-2}, the absorbed dose continues to decline. As explained above, the dose does not drop to zero at the maximum range due to the presence of secondary particles, such as electrons and ions that can deposit energy far downstream of the incident's particle range.

An examination of the fluence calculations explains this observation. Figure 4 shows the fluence of oxygen and smaller ions for the selected simulation. Virtually all of the oxygen ions have stopped by the time they reach 25 g cm^{-2} in the water target. Below 25 g cm^{-2}, a small number of ions between Z=3 and Z=7 are formed as a result of fragmentation, but these ions are

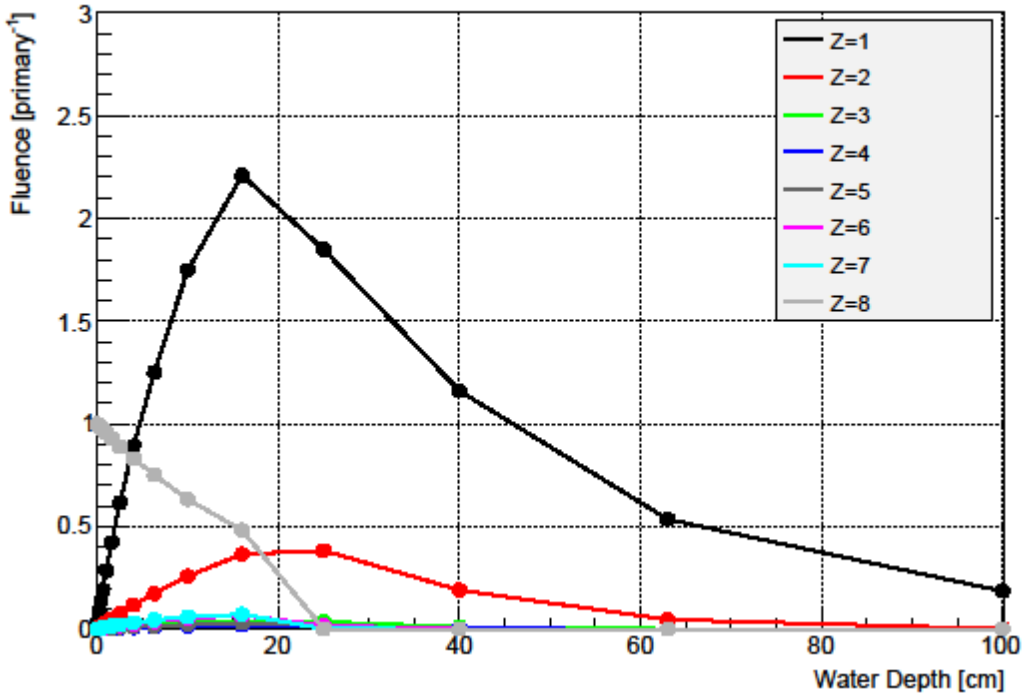

Figure 4: Fluence Curves for Z=1 to Z=8 for 400 MeV/n Oxygen Ions Incident on a Water Target behind 0.004 g cm^{-2} Al and 0.0063 g cm^{-2} Poly

created infrequently. Much larger quantities of protons and alphas are created, reaching a maximum of 2.2 protons per primary at 16 g cm^{-2} and 0.38 alphas per primary at 25 g cm^{-2}. As Figure 2 illustrates, the absorbed dose drops quickly following the peak at 16 g cm^{-2} as a result of the oxygen ions' reactions between 16 and 25 g cm^{-2}. From 25 g cm^{-2} through the rest of the target, the energy deposition is dominated by the secondary protons and alphas.

A comparison of the dose and dose equivalent of the different particles illuminates the significance of the energy deposited by incident particles when they have almost reached their maximum range in the water shield. Figure 5 and Figure 6 show absorbed dose and dose

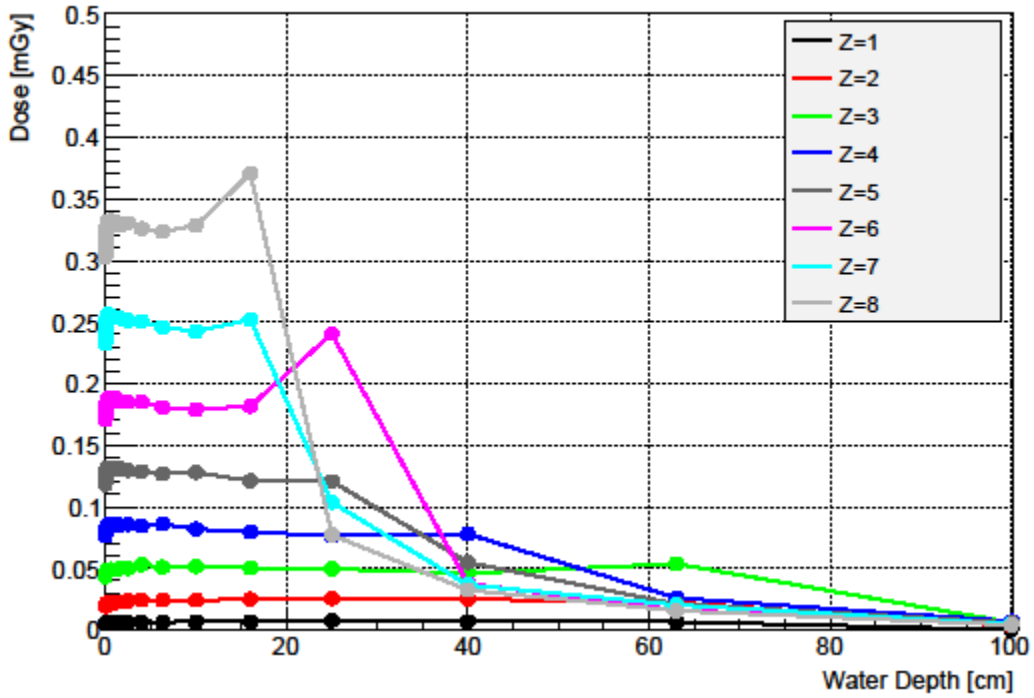

Figure 5: Absorbed Dose v. Depth for Ions from Z=1 to Z=8 for a Water Target Shielded by 0.004 g cm^{-2} Al and 0.0063 g cm^{-2} Poly

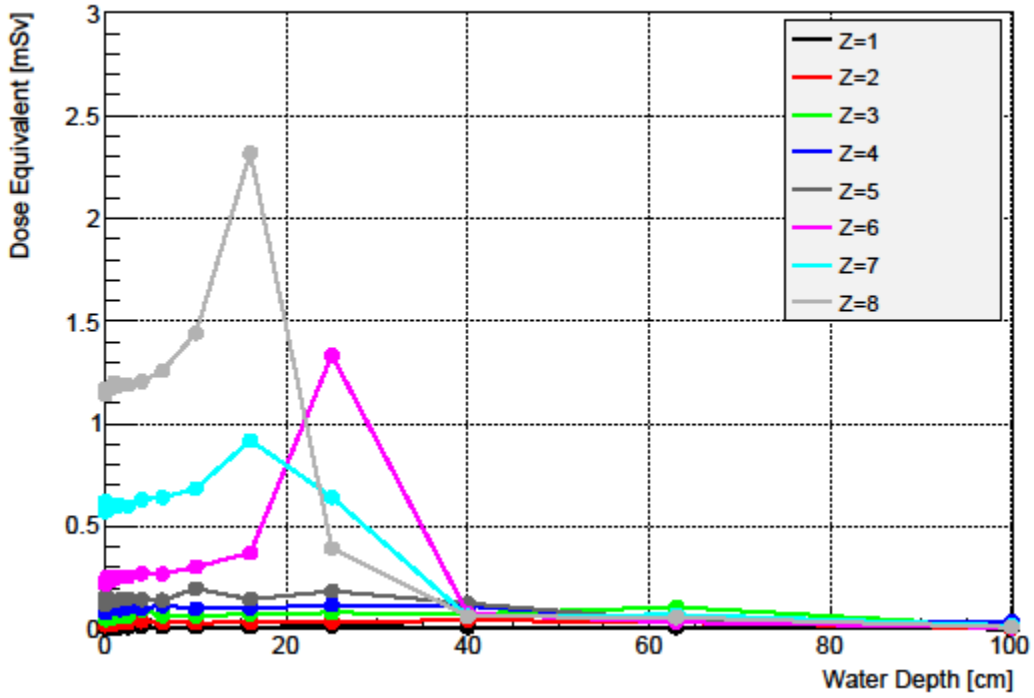

Figure 6: Dose Equivalent v. Depth for Ions from Z=1 to Z=8 for a Water Target Shielded by 0.004 g cm^{-2} Al and 0.0063 g cm^{-2} Poly

equivalent plotted against depth in the water target for the shielding combination described above for particles from Z=1 to Z=8 (protons to oxygen ions). Several observations can be made from these figures. First, as Z increases, the range of the particle decreases, and the height of the maximum dose and dose-equivalent deposition rises. These results are not surprising because the stopping power is proportional to z^2 and the larger ions at the same velocity have more energy. At 400 MeV/n, the alphas have 1,600 MeV of kinetic energy where the protons have only 400 MeV. Second, at this shielding combination, well-defined peaks do not appear for the particles with Z less than 6. These particles appear to deposit their energy more evenly than the larger particles. As the smaller particles occur with greater frequency in the GCR spectrum, it is

expected that this characteristic will lead to relatively flat depth-dose curves compared to the large variations that occur as a result of the large ions. Third, the dose equivalent curves in Figure 6 show that the biological damage that results from these peaks is significant. For example, the oxygen peak at 16 g cm^{-2} exceeds the dose equivalent for the protons and alphas by an order of magnitude.

V. Application of the FLUKA Lookup Tool to the CRaTER Telescope

A. The CRaTER Telescope

1. Characteristics of the CRaTER Telescope

The primary purpose of the CRaTER instrument is "to characterize the global lunar environment and its biological impacts" (Ref. 27). Although the impacts of radiation on earth and in low earth orbit are comparatively well known, the radiation environment in deep space and near the Moon (i.e., outside of Earth's protective magnetic fields) is not as well understood. In essence, the CRaTER instrument consists of an array of silicon detectors (described in more detail below) both in front of and behind aluminum shielding and tissue-equivalent plastic, which is intended to simulate the human body. The CRaTER project intends to produce a linear energy transfer spectrum for observed GCR and SPE spectra by measuring the loss of energy of incident radiation in each detector. The detectors are designed to produce a signal in proportion to the energy loss in the detector. Dividing the energy loss (ΔE) of the particle in question by the length of the silicon detector (L) provides an estimate of the linear energy transfer (LET) imparted by the incident particle (Ref. 27):

$$LET=\Delta E/L$$

The CRaTER detector is located on the Lunar Reconnaissance Orbiter ("LRO") spacecraft. As discussed by Spence *et al.* (Ref. 27), two of the LRO measurement objectives relate directly to CRaTER:

> The LRO shall characterize the deep space radiation environment at energies in excess of 10 MeV in lunar orbit, including neutron albedo.

> The LRO shall measure the deposition of deep space radiation on human equivalent tissue while in the lunar orbit environment.

Moreover, CRaTER has an "exploration goal" of "provid[ing] the first deep space validation of radiation transport models" (Ref. 27). Specifically, the CRaTER collaboration intended to compare experimental data from CRaTER to LET spectra produced using HETC-HEDS and HZETRN.

The CRaTER telescope is designed as follows. A simplified illustration is shown in Figure 7. The zenith side of the telescope generally faces deep space, and the nadir side of the telescope faces the lunar surface, although the LRO occasionally shifts its orientation in the conduct of its missions. A particle incident on the zenith side of the telescope traverses the following regions of the telescope, in order. First the particle penetrates the zenith shield, which consists of 812.8 μm of aluminum. Immediately behind the zenith shield are two silicon detectors. A thin detector (D1) is followed by a thick detector (D2). Then, the particle enters the first region of tissue-equivalent plastic ("TEP"), followed by another set of thin (D3) and thick (D4) detectors. After exiting detector D4, the particle enters the second region of TEP, followed by the final pair of detectors (D5 and D6). As with the other detectors, D5 is thin and D6 is thick. Behind D6 is the nadir shield, 810.3 μm of aluminum, which comprises the end of the telescope.

In determining the geometry and size of the CRaTER telescope, the collaboration considered "the total pathlength through TEP desired, the sizes of the different pieces of TEP, and the geometric factor and resulting sensitivity of the entire telescope" (Ref. 27). With respect

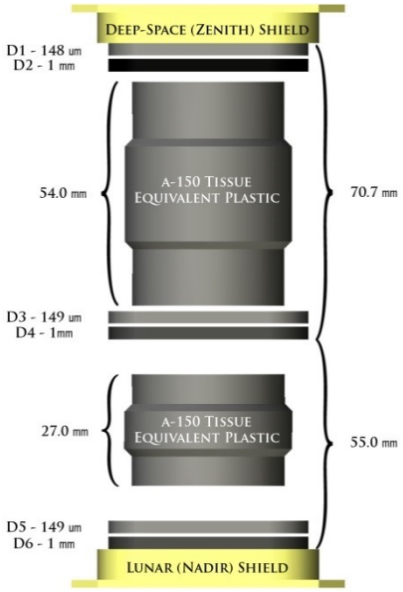

Figure 7: Schematic drawing of the CRaTER instruments. (From http://crater.sr.unh.edu/instrument.shtml)

to the design of the TEP, the CRaTER team determined the thickness of the first region of TEP such that 100 MeV protons are just able to exit the first TEP region, which occurs at approximately 60 mm of TEP. CRaTER is designed with a total length of TEP of approximately 81 mm. The first region of TEP (closest to the zenith side) is approximately 54 mm long, and the second region (closest to the nadir side) is approximately 27 mm long. The CRaTER collaboration found that this combination of lengths (2/3 and 1/3) provided "a useful combination of lengths, also similar to typical thicknesses through human tissue to depths of blood forming organs" (Ref. 27).

As mentioned, CRaTER's detectors are paired, with one thin detector followed by one thick detector in each group. The thin detectors are approximately 150 microns thick, and the thick detectors are approximately 1000 microns thick. Paired thick and thin detectors are

necessary to characterize the LET of incident radiation across the large range of LET that is observed from SPE and GCR.

CRaTER's geometry was selected by considering the necessary event rate to characterize the changing features of the GCR and SPE spectrum. Calculations showed that a minimum geometric factor (D1-D6) of 0.57 cm^2 sr would result in approximately 1,000 events per hour at solar minimum, which is sufficient to detect and characterize changes in the GCR spectrum, which changes relatively slowly. A trade study considered the relative benefits of a wider detector (larger geometric factor), which would allow for the collection of more data but could result in complications during SPE, when particle fluxes become high. Specifically, pulse pileup in D2 as the result of the extremely high proton fluences during SPE counseled against a larger geometric factor.

To simulate human tissue, the CRaTER telescope employed Exradin TEP A-150. The A-150 TEP used in the CRaTER telescope is comprised of 10.33% hydrogen, 76.93% carbon, 3.30% nitrogen, 6.93% oxygen, 1.14% fluorine, and 1.37% calcium by weight, with a density of 1.127 g cm^{-3} (Ref. 27). The zenith section of the TEP was 53.992 mm long, and the nadir section was 26.972 mm long. The aluminum endcaps used on the CRaTER telescope were 812.8 μm at the zenith and 810.3 μm at the nadir. The endcaps were made of Al 6061-T6, which is comprised of 97.2% elemental aluminum.

Importantly, the CRaTER telescope underwent extensive calibrations prior to embarking on the LRO. Prior to the completion of assembly, the individual pairs of detectors were calibrated using radionuclide sources such as cobalt-60 and americium-241. This step was

performed prior to final assembly because it is not possible to stimulate the detectors with radionuclide sources following detector assembly. Also, radionuclide sources produce well-defined energy spectra, greatly aiding in the calibration process. Following assembly, CRaTER was calibrated using protons beams of energies up to 230 MeV at the Northeast Proton Therapy Center at Massachusetts General Hospital (Ref. 27). CRaTER was also calibrated at the 88" cyclotron at Lawrence Berkeley National Laboratory utilizing ions beams ranging from protons to Bismuth with energies up to 30 MeV/n (Ref. 21). Finally, a characterization study was performed at the NASA Space Radiation Effects Laboratory at Brookhaven National Laboratory. This study used proton, silicon, iron, and chlorine ion beams at energies ranging from <300 to 1000 MeV/n (Ref. 27).

2. Existing CRaTER Simulations

Both Monte Carlo and deterministic codes have been used to model energy deposition and fluence within the CRaTER instrument. Porter *et al.* (Ref. 21) have performed a comparison of HZETRN and HETC-HEDS calculations with actual data available from the CRaTER instrument for an 18-month period (June 29, 2009 to December 31, 2010). Porter's recent work examines separately the contributions by primary and secondary ions that are capable of penetrating the entire CRaTER instrument (D2/D4/D6 triple coincidence) from the instrument's zenith end. The contributions of particles that were not energetic enough to deposit energy in all detectors were not included in the calculations. The paper compares a calculation of LET in detectors D1 and D2 with data obtained from CRaTER.

Porter modeled the GCR spectrum in HETC-HEDS by performing calculations for ions from protons (Z=1) to iron ions (Z=26). Simulations were run at several energies ranging from 20 to 3,000 MeV/n. Porter used an average LET calculated in each detector by dividing the energy lost by each particle by the thickness of the detector:

$$Average\ LET = \sum_{i=1}^{n} \frac{(E_{initial} - E_{final})_i}{n\,L}$$

where n represented the number of histories, i represented the particle being calculated, L was the thickness of the detector, $E_{initial}$ was the energy of the particle as it entered the detector, and E_{final} was the energy of the particle as it left the detector. (Ref. 21). Even for proton simulations, a wide range of secondary particle identities and energies made the determination of secondary LET contribution challenging. For example, secondaries from 1-3 GeV/n protons included secondary protons, neutrons, and all species of pions and muons. To simplify these calculations, Porter obtained LET by averaging.

Porter found generally good agreement for high LET values between data from CRaTER and HETC-HEDS calculations. Isolating the contributions of secondary particles revealed that many of the peaks that appear in the HETC-HEDS calculation that do not correspond to observed data result from HETC-HED's simulation of secondary particles. With respect to the HZETRN calculation, Porter also found generally good agreement with the exception of the proton and alpha peaks. Comparing the HZETRN and HETC-HEDS calculations, Porter finds that the treatment of secondary particles in HETC-HEDS accounts for most of the differences (Ref. 21).

B. Building the Spectrum

The lookup tables described above produced a table of dose, dose equivalent, and particle fluences for a given particle type and energy. These results must be folded into a SPE or GCR spectrum to be of practical value, as space radiation does not consist of one type of monoenergetic particles. Rather, GCR and SPE spectra consist of a wide variety of particles at a wide range of energies. To create a spectrum, it is necessary to fold the calculations for individual particles and energies into a fluence spectrum. When the particles are multiplied by their fluences for a given spectrum, the results can be added together to obtain an estimate of the energy deposition and fluences for the observed spectrum.

For the purposes of these comparisons, the GCR calculations of Badhwar and O'Neill were used (Ref. 35). Although a more recent update to the code was promulgated in 2011, the 2010 version of the code (Ref. 26, 35) was used for these calculations to ensure consistency with the HZETRN and HETC-HEDS to which the results of these calculations will be compared. The BO'10 code provides an approximation of the GCR spectrum in the heliosphere as a function of solar activity. BO'10 assumes an influx of particles into the heliosphere that is constant in both identity and energy of particles. This spectrum is termed the Local Interstellar Spectrum. Starting from a constant Local Interstellar spectrum, BO'10 uses the Focker-Planck Equation to calculate the GCR spectrum at a given point in the heliosphere. The Focker-Planck Equation relies exclusively on the solar modulation parameter (Φ), which estimates the sun's modulation of GCR, to account for the activity of the sun in attenuating GCR flux. BO'10 relies on the International Sunspot Number to estimate Φ. The BO'10 code gives the user the option of

inputting either a date range or a value for Φ and will return the GCR spectrum for particles from Z=1 to Z=94 at energies ranging from 1 to 10^6 MeV/n (Ref. 15).

The BO'10 code provides the energy distribution for each particle for a given Φ. The GCR spectrum for each particle is continuous in energy, but the available lookup tables with the calculations from these simulations are discrete. BO'10 produces a spectrum binned at discrete intervals, which must then be converted to an appropriate binning for use with the available calculations. To use the BO'10 spectrum, it is necessary to convert the spectrum values returned by the code to appropriate bins based on the energies available for the FLUKA calculations. This task was accomplished using a cubic Lagrangian interpolation in most cases (Ref. 36). In the event that the cubic interpolation resulted in values that were outside the range of the next lower and higher BO'10 point, a linear interpolation was used instead. Using this interpolation technique, binned spectra were obtained for each particle. Figure 8 illustrates the GCR spectrum calculated by BO'10 and the points used to produce the FLUKA lookup tool.

As described above, the BO'10 code calculates the spectrum for particles up to plutonium (Z=94) and energies up to 10^6 MeV/n (Ref. 35). However, the FLUKA calculations performed in these simulations extend only up to iron (Z=26) and 10^4 MeV/n. The comparisons performed for this work neglect particles heavier than iron (Z=26) and more energetic than 10^4 MeV/n. Generally, the incident flux of these heavier and more energetic particles is so low that they do not contribute meaningfully to the fluence, dose, and dose equivalent calculations of these simulations. In some instances where direct comparison is made to existing codes where calculations above 5 GeV/n were not performed, the 10 GeV/n data was not used for the sake of

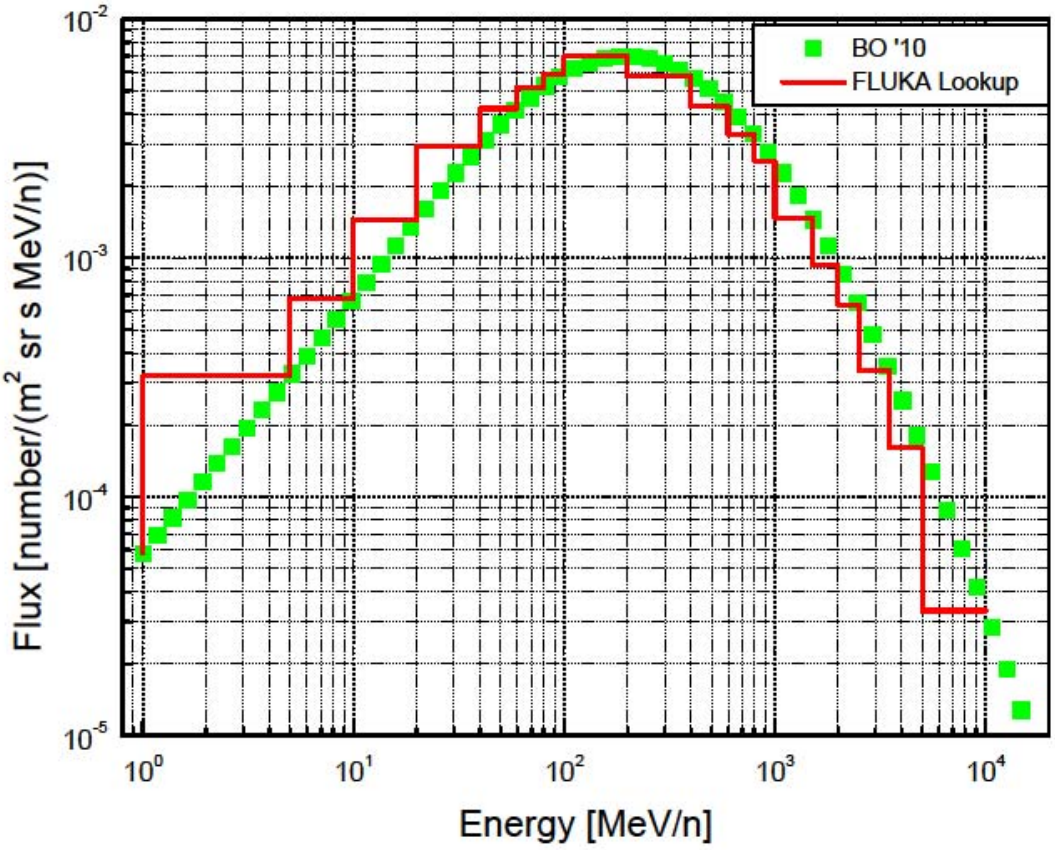

Figure 8: GCR Flux v. Energy for Oxygen Ions.

consistency with the prior calculation.

After selecting a period for comparison, obtaining a spectrum and calculating results for the spectrum were a relatively straightforward matter. The analysis performed by Porter examined data from CRaTER taken from June 29, 2009 to December 31, 2010 (Ref. 21). Inputting these dates into BO'10 produces a solar modulation parameter (Φ) of 507.5996 MV for this period and produces the calculated spectrum, neglecting flux values from more than 10 GeV/n or particles heavier than iron.

From this step, additional corrections were manually made to the spectrum to adjust for the parameters of the experiment. Porter's HETC-HEDS and HZETRN comparisons consider only detector events that meet triple coincidence criteria. The use of triple coincidence means that only particles that are energetic enough to deposit energy in all three detector pairs are recorded. The incident particles or a secondary particle must penetrate approximately 10 g cm^{-2} of CRaTER to trigger events in all three detector pairs. This coincidence requirement means that the lowest energy particles are not recorded because they will not deposit energy in all three detectors. Inclusion of these particles would cause systematic error in the zenith portions of the detector, where the lower energy particles would contribute to the total energy deposition, but these results would not be recorded by the CRaTER data or other simulations. To correct for this phenomenon, the BO'10 spectra below the threshold energies for each particle were set to zero, as they were in the HETC-HEDS calculation (Ref. 21). The threshold energies for each particle are listed in Table 6. These values are the same as those used by Porter *et al.* (Ref. 21). These values are consistent with the values observed for the FLUKA calculations and because Porter calculated values every 5 MeV/n in this energy range rather than every 20 MeV/n, as the lookup tool does. In cases where the threshold energy fell between calculated points for the FLUKA lookup tool, the fluence of the calculation containing the threshold energy was prorated linearly. For example, Porter's threshold for lithium ion is 45 MeV/n. For the FLUKA calculation, the 40 MeV/n point is excluded, and the 60 MeV/n point is included, but its fluence is reduced by one quarter to account for the fact that particles between 40 and 45 MeV/n would not meet the triple

Table 6: Threshold energies for each particle (Ref. 21). Below these energies, the BO'10 spectrum was set to zero.

Z	Threshold E (MeV/n)
1	100
2	65
3	45
4	35
5	30
6	35
7	35
8	40
9	30
10	30
11	40
12	60
13	30
14	30
15	30
16	65
17	30
18	30
19	35
20	35
21	30
22	30
23	30
24	30
25	30
26	50

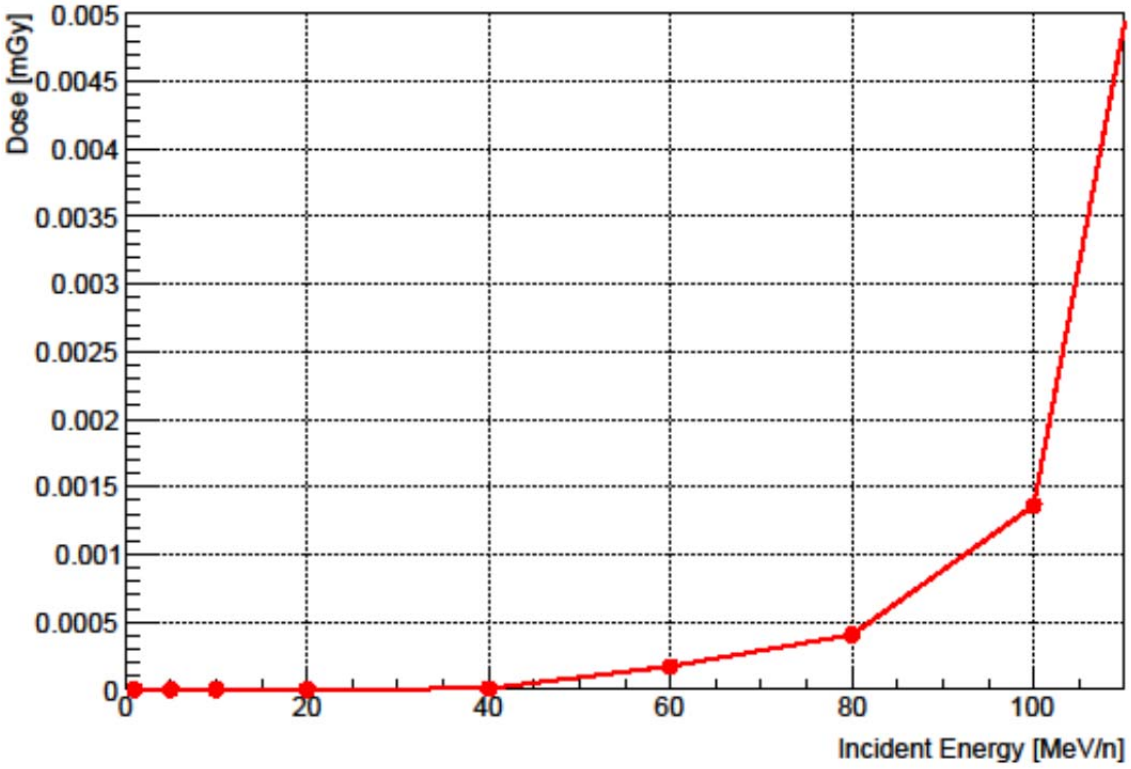

Figure 9: Dose v. Incident Energy for ^{7}Li ions.

coincidence criteria. As explained earlier, the BO'10 fluence value for the 60 MeV/n datum accounts for the fluence between 40 and 60 MeV/n. Figure 9 shows the dose deposited by incident ^{7}Li ions and illustrates the implementation of the minimum energy for triple coincidence of 45 MeV/n.

It is important to understand when comparing dose and dose equivalent data calculated in this fashion that the calculations cannot be substituted for physical dose and dose equivalent calculations. Heavy ions typically deposit the majority of their energy at the end of their trajectories. If the low energy ions that do not penetrate all three sets of detectors are excluded,

the calculated dose and dose equivalent in the zenith sections of the telescope do not correspond to the actual dose and dose equivalent deposited at this points. In fact, they exclude the particles that are likely the largest contributors to the dose at these locations.

The allocation of the fluence from the BO'10 code introduces error into this simulation of the CRaTER telescope in at least two ways. First, this simulation allocates the fluence for a given energy bin uniformly between the energy deposition calculated at the high and low endpoints. Using 100 MeV/n lithium ions as an example (shown in Figure 9), the calculated BO'10 fluence for the 100 MeV/n point accounts for all of the lithium fluence in the given GCR spectrum between 80 MeV/n and 100 MeV/n. This fluence value is spread evenly between the calculated energy deposition values for the 80 MeV/n and 100 MeV/n points. However, Figure 9 shows that the deposition of energy is not uniform between these energies. Some error is introduced as a result of running the calculations at only certain energy values and assuming that the energy deposition is uniformly distributed between them.

Second, another source of possible error in the building of these spectra is the use of the most abundant isotope for each particle. For example, for Z=1, the simulations treat all incident particles as protons. However, the GCR spectrum includes deuterons and tritons as well. Similar to the discussion above, the exclusion of these isotopes may either exaggerate or minimize the impact of an interaction that occurs in the other ion because the less abundant isotopes were not calculated.

A ROOT (Ref. 37) macro was used to fold the spectrum into the lookup tables for the energy deposition data. The macro resulted in a new lookup table that shows the dose and dose equivalent at the given depths of water for an aluminum-polyethylene shielding combination.

C. Modeling the CRaTER Telescope

In order to use the FLUKA lookup tool to create an accurate model of the CRaTER telescope, it was necessary to select materials and material thicknesses that are commensurate with the dimensions of CRaTER. While the CRaTER telescope has approximately 0.23 g cm^{-2} of Al in the zenith shield, the lookup tables did not model 0.23 g cm^{-2} of Al shielding. Rather, the lookup table calculations consider 0.16 g cm^{-2} of Al and 0.25 g cm^{-2} of Al. Although consideration was given to a spline or a weighted average for the precise amount of aluminum, the decision was ultimately made to simply model the zenith shield as 0.25 g cm^{-2} of Al. The difference between 0.23 g cm^{-2} of shielding and 0.25 g cm^{-2} of shielding is not significant, and attempting a weighted average or interpolation between 0.25 g cm^{-2} and 0.16 g cm^{-2} of Al would not significantly improve the accuracy of the calculation. The materials behind the zenith shield (i.e., the rest of the telescope) were modeled as 100 g cm^{-2} of water. Although the CRaTER telescope is only about 10 g cm^{-2} thick, the lookup tables all used 100 g cm^{-2} of water, so this is the data that is available. Of course, the CRaTER telescope is made of A-150 TEP and silicon detectors rather than water, but water was the best choice of materials available from the lookup tables. Energy deposition in silicon detectors is often simulated with the deposition of energy in water, and TEP is intended to simulate human tissue, which is also routinely simulated with

water. The aluminum in the nadir shield is not simulated because the lookup tables did not include calculations where aluminum was placed behind the water column. It is expected that a high-Z material such as aluminum will result in some back-scatter into the telescope. Because the FLUKA simulations did not simulate a second layer of aluminum, we assume for the purposes of these calculations that the nadir shield is not present. The FLUKA calculations were performed in 100 g cm^{-2} of water, so the thickness of the water in the simulation of the CRaTER is approximately ten times that of the CRaTER telescope. As with the aluminum shield, we neglect the presence of the downstream water in our model of the telescope.

Neglecting the nadir shield and including 90 g cm^{-2} of water behind the CRaTER detector does not have a large impact on the accuracy of the model. Based on the isotropic nature of the GCR spectrum, one may expect that these approximations would significantly affect the outcome. However, the triple-coincidence require of the CRaTER telescope ensures that particles entering the telescope laterally are unlikely to be counted. Furthermore, in the simulations, all particles are incident axially from the zenith end, so the downstream materials only make a difference to the extent that they affect backscatter.

D. Deposition of Energy in the Detector

One additional factor that must be considered in formulating a calculation of the CRaTER detector is the location and size of the detectors in CRaTER vis-à-vis the simulated detectors in the FLUKA simulations. As described above, the detectors in CRaTER consist of a thin and thick detector pair (Ref. 27). The FLUKA simulations consist of detectors that are

uniformly 1 μm in thickness. It is well-known that the simulation of detectors is influenced by the thickness of the detector (Ref. 38). Therefore, the difference in thickness between the detectors involved in the CRaTER simulation and the FLUKA simulation will insert some error into the calculations.

This error will derive primarily from two sources. First, because the CRaTER detectors are thicker than the FLUKA simulation detector, the energy deposited in them by the incident radiation will take place over a wider depth. Therefore, the CRaTER detector energy depositions will encompass a wider range of LET than the FLUKA simulations. The LET of charged particle radiation changes rapidly at some points in the charged particle's trajectory, so depending on the particle, the lineal energy deposited in the wider detector may differ from the lineal energy deposited in the narrower detector.

Second, the lineal energy calculated using a Monte Carlo code follows the mean energy deposition in the detector, but the responsiveness of the physical detector tracks the most probable deposited energy. The energy deposited in the detector generally follows the Vavilov distribution (Ref. 38). For the Vavilov distribution, the mean energy deposition is greater than the most likely energy deposition due to the tail of the Vavilov distribution for infrequently occurring but high energy loss events. Therefore, a Monte Carlo dose calculation is expected to overestimate the values that would be physically measured in the CRaTER detector. Zeitlin has examined this effect for the CRaTER detectors and has formulated an equation to calculate the most probable energy loss for high-energy protons:

$$\Delta_p = t(190 + 16.3 \ln t)$$

where t is the thickness of the detector in μm and Δ_p is the most probable energy loss in eV (Ref. 39). While the mean energy loss is approximately the same regardless of detector size, the magnitude of this shift becomes more severe as the silicon detector gets thinner. For particles larger than protons, it is expected that the most probable energy loss will increase approximately as a factor of z^2 (Ref. 39). However, this information is of limited usefulness for heavier ions because the heavier ions produce secondaries and fragments that also cause energy deposition. Without a close examination of the identity of the particles causing the energy deposition, it is not possible in all cases to determine the necessary correction.

In addition to the effects of the detector's thickness and width, the location of the detectors will insert some error into the calculation. The calculated energy deposition points in the FLUKA simulations do not match the location of the detectors in the CRaTER telescope; therefore, it was necessary to select points from the FLUKA simulations that most closely matched the points from the CRaTER telescope. For the D1 and D2 detectors, which are the primary detectors of interest in this work, the FLUKA simulations used the detectors located at 0.0063 cm and 0.063 cm for detectors D1 and D2 respectively. These detectors were selected because they were the closest to the center of D1 and D2.

E. Calculating Lineal Energy (y) from FLUKA DOSE

As described in more detail above, the FLUKA lookup tool results provide energy deposition calculations for the deposition of energy in water. In order to compare calculations of the CRaTER instrument with existing data and calculations, it is necessary to convert the

calculated absorbed dose in water from the lookup tool to an LET spectrum in silicon, which best simulates the behavior of the detectors on CRaTER.

Starting with the absorbed dose in water, the first step is to convert the absorbed dose in water (D H_2O) to LET in water (LET_∞ H_2O). As described above, Monte Carlo simulations such as FLUKA do not directly calculate dose, which is a point quantity. The simulation actually calculates the average dose in the detector rather than the point dose at a particular location in the detector. Just as dose is a point quantity, LET is also a point quantity. The "average LET" across the entire detector is actually the lineal energy (y). The lineal energy can be calculated from the detector dose as follows:

$$y = \frac{\rho \times \bar{D}}{\varphi}$$

where ρ is the density of the detector, D is the cumulative dose in the detector, and φ is the fluence across the detector. Therefore, the following calculation was used to obtain lineal energy from the raw FLUKA DOSE data:

$$y\left(keV/\mu m\right) = \frac{D\ GeV}{g} * \frac{10^6\ keV}{GeV} * \frac{1\ g}{cm^3} * \frac{\pi * 10^{10} cm^2}{} * \frac{cm}{10^4 \mu m}$$

The second step of the conversion is to use the calculated value of LET_∞ H_2O to find LET_∞ Si, which is representative of the energy deposited in the CRaTER detectors. Several approaches to this conversion are possible to convert from LET_∞ H_2O to LET_∞ Si. As Benton *et al.* have explored (Ref. 40), most researchers simply select a conversion constant to convert from LET_∞ H_2O to LET_∞ Si. Noting that the selection of conversion constants is not consistent between researchers even for the same underlying data, Benton found this approach lacking and

instead developed an empirical functional relationship between LET_∞ H_2O and LET_∞ Si. Exploring this relation for ions from Z=1 to Z=26 and ranging in energies from 0.8 MeV/amu to 2000 MeV/amu, Benton found a ~30% difference in the ratio LET_∞ H_2O/LET_∞ Si over the entire range of energy for all Z, indicating that a constant multiplier could result in significant systemic error. From 0.8 MeV/amu to 50 MeV/amu, the ratio ranges from approximately 0.52 at 2000 MeV/amu to 0.72 for ^{56}Fe ions at 0.8 MeV/amu. Notably, the ratio drops to 0.55 at ~50 MeV/amu, so the variation of the ratio is only ~5% from 50 MeV/amu to 2000 MeV/amu, while it is ~30% for the entire energy range (Ref. 40).

Benton also observed significant differences based on particle identity at the lower end of the spectrum (below ~50 MeV/amu). For example, near the lowest energy (0.8 MeV/amu), a ratio of 0.65 was observed for protons while 0.72 was observed for ^{56}Fe ions. The curves for each particle tended to converge at approximately 50 MeV/amu, where the ratio is approximately 0.55 (Ref. 40).

Using empirical data, Benton fitted a curve to relate the LET in water to the LET in silicon:

$$\log(\mathrm{LET}_\infty\ \mathrm{H_2O}\ ) = -0.2902 + 1.025\log(\mathrm{LET}_\infty\ \mathrm{Si}\ )$$

Although Benton "make[s] no claims regarding the rigor or quality" of this functional relationship, he states that use of this relationship "must certainly yield better results than the use of a single numerical constant" (Ref. 40). FLUKA collaborators, specifically Golightly, have adopted this approach for conversion between LET_∞ H_2O and LET_∞ Si (Ref. 41).

F. Binning of Calculations

The CRaTER experimental data was binned first using the ADC bin values, which were calibrated to energy as the result of several experiments, described previously. Then, the CRaTER experimenters combined the bins by establishing count minima for each bin. If the required number of counts was not obtained, then bins were combined until the minimum was reached. For the thick detector region, the minimum was 5,000 counts. For the thin detector region, the minimum was 1,000 counts. Case et al. chose these values "by visually inspecting the spectra and balancing the decrease in statistical uncertainty with the decrease in energy resolution" (Ref. 8).

In order to replicate the CRaTER experimental data as closely as possible, it was decided to mimic the binning structure of the CRaTER experimental data, as reported (Ref. 8). This approach allows a point-by-point comparison of the calculations to the reported experimental data and reduces the possible confounding of the comparisons formed by disparate bin structures. The direct application of the technique (rather than the replication of the binning structure) used by Case et al. is inappropriate for two reasons. First, the experimental data were collected over the full continuum of space radiation, whereas the simulated data were only collected for discrete energies for certain points. Therefore, applying the same binning technique could make the reported calculations more dependent on the application of the binning structure than the calculations themselves. Preserving the binning structure of the experimental data helps to ensure that the peak structures apparent in the experimental data are not obscured by the use of a different binning structure.

Second, the selection of energy values for the calculation is arbitrary and not based on the physical phenomena. The energies selected for the FLUKA runs were not in any way based on expected energy depositions in the CRaTER detector. Therefore, any efforts to replicate the binning technique used by the CRaTER collaboration would establish bins based on where the energy values for the primaries were chosen rather than the features of the lineal energy distribution.

Based on these considerations, the FLUKA calculations were binned according to the same binning structure that was used for the experimental data. However, in calculating the fluence within each bin, some bins contained no fluence. Because these zero fluence bins are an artifact of the energy selections and the energy cutoff, the zero points were excluded from the comparison.

Another important consideration in plotting the FLUKA data was where to locate the fluence for each calculated data point. The fluence numbers calculated by the BO'10 account for the range of energy from the next lower energy point to the named point. Using the FLUKA energy values as an example, the 1 MeV/n fluence value accounts for the fluence between 0 MeV/n and 1 MeV/n. The next higher bin is 5 MeV/n, and this fluence value accounts for the fluence between 1 MeV/n and 5 MeV/n. The highest FLUKA bin that was calculated was for 10 GeV/n, which would encompass all of the fluence between the next lower energy (5 GeV/n) and 10 GeV/n. Therefore, the highest energy bin accounts for half of the energy spectra over which the FLUKA simulations were run. This characteristic is problematic because it results in an inaccuracy by placing all of the fluence to be plotted at a particular lineal energy when the

fluence should in fact be spread over a range of lineal energies, based on the next lower energy, which is, generally, the next higher lineal energy. In many cases, the reported fluence for a given energy should be spread among three or more lineal energy bins. Placing the entire fluence into a single bin inserts several physically meaningless peaks into the plotted data. To account for this difficulty, it is assumed that the fluence for a given energy is uniformly distributed between the lineal energies of the data point for the energy values for which the fluence values account. If this range extends to multiple bins, the fluence is prorated among the bins in proportion to the overlap between the lineal energy range and the bin width.

For example, Table 7 shows the calculated lineal energy and fluence values for oxygen ions that are incident upon 0.25 g cm^{-2} of aluminum and 100 g cm^{-2} of water, which simulates the CRaTER detector. The column labeled Energy is the incident energy of the ion for which the simulation was run, the Lineal Energy column shows the lineal energy that was calculated from the DOSE calculation, and the Fluence column shows the BO'10 fluence that falls between the incident energy and the next lower energy. The low-energy fluences are adjusted to account for the triple coincidence requirement described above. Therefore, all fluences below 40 MeV/n were set to zero. Taking the 80 MeV/n bin as an example, the fluence of 0.104 day^{-1} cm^{-2} sr^{-1} accounts for the BO'10 fluence between 60 and 80 MeV/n. Therefore, we consider this fluence as being uniformly distributed between lineal energies of 62.1 and 80.5 keV/μm. An examination of the

Table 7: Lineal energy and fluence values calculated for oxygen ions incident upon 0.25 g cm^{-2} of aluminum and 100 g cm^{-2} of water, simulating the CRaTER detector

Energy (MeV/n)	Lineal Energy (keV/μm)	Fluence (#/(day cm^2 sr))
1	0.000	0.000
5	0.000	0.000
10	0.001	0.000
20	0.062	0.000
40	129.286	0.000
60	80.478	0.084
80	62.089	0.104
100	51.644	0.117
200	30.932	0.695
400	20.907	1.146
600	17.653	0.862
800	16.116	0.656
1000	15.327	0.508
1500	14.581	0.735
2000	14.026	0.467
2500	14.043	0.318
3500	14.025	0.336
5000	14.013	0.242
10000	15.211	0.167

Table 8: Distribution among bins for the calculated value for 80 MeV/n oxygen ions

y (low)	y (high)	y (range)	y (covered)	Fluence
58.9	63.5	4.6	1.4	0.008
63.5	67.8	4.3	4.3	0.024
67.8	72.2	4.3	4.3	0.024
72.2	77.5	5.4	5.4	0.030
77.5	84.7	7.1	3.0	0.017

CRaTER data's bins reveals five different bins that encompass this range of lineal energy, spanning roughly from 58-63, 63-67, 67-72, 72-77, and 77-84 keV/μm (Ref. 8). Table 8 shows how the 80 MeV/n calculated value is divided among these bins. If the fluence were not distributed over these five bins, the entire value would have been plotted in the 58-63keV/μm bin, overstating the fluence in this bin by an order of magnitude while understating the fluence in the four other bins.

G. Development of a Closer Model of the FLUKA Telescope

In order to explore the efficacy of the lookup tables more thoroughly, it was necessary to develop a model of the CRaTER telescope in FLUKA that more closely resembles the CRaTER instrument. The model of the CRaTER telescope more accurately depicts the geometry of the telescope, simulates the materials found in the telescope rather than using water as a proxy for both the silicon and the TEP, and places detectors at the appropriate locations to simulate all six detectors on board CRaTER.

There are several advantages to performing this calculation. First, creating a more accurate model of the CRaTER telescope allows for an analysis of the impact of the assumptions made in applying the lookup tool to CRaTER as opposed to differences that result from

FLUKA's physical models. The relevant lookup tables contain calculations for aluminum-shielded water. However, CRaTER's interior is made of silicon and TEP rather than water. Performing a more direct simulation of CRaTER could isolate problems that arise from the substitution of materials. Moreover, the dimensions and locations of the detectors in the lookup tables are not the same as those found in CRaTER. Second, and most important, the purpose of this research is to examine to what extent a simplified lookup table can be used to simulate experimental phenomena. A comparison of the lookup table calculation to the experimental data shows both the limitations of FLUKA and the limitations of the lookup table methodology. If this more direct simulation of the CRaTER detector is robust, then a comparison of the lookup table calculation to the direct CRaTER simulation will isolate the loss of accuracy due to the lookup table methodology from the choice of the FLUKA code.

The model developed for this simulation did not account for the isotropic nature of the GCR spectrum, however. Although placing the incident particles isotropically around the detector would more closely simulate the GCR incident on CRaTER, it creates additional difficulties in simulating the triple coincidence of the detectors. As explained above, the triple coincidence of the detectors is simulated by eliminating particles from the spectrum that do not possess enough kinetic energy to penetrate the entire detector. The vast majority of particles that are able to meet the triple coincidence requirement will enter approximately axially through the zenith shield. Simulating all particles as entering the detector axially and at the center captures

Table 9: Geometry used in the calculation to simulate the CRaTER detector (Ref. 27)

Component	Material	Length (cm)	Cumulative Length (cm)
Zenith Endcap	Al	0.08128	0.08128
D1	Si	0.01480	0.09608
D2	Si	0.10000	0.19608
TEP 1	TEP A-150	5.39670	5.59278
D3	Si	0.01490	5.60768
D4	Si	0.10000	5.70768
TEP 2	TEP A-150	2.69800	8.40568
D5	Si	0.01490	8.42058
D6	Si	0.10000	8.52058
Nadir Endcap	Al	0.08100	8.60158

the most significant contributors and preserves a straightforward means of applying the triple coincidence requirement.

For the purposes of this simulation, the CRaTER telescope was simulated as a cylinder that is 1.7480775 cm in radius with the axial lengths shown in Table 9. The detectors were simulated as pure Silicon, and the endcaps were simulated as pure aluminum. The TEP regions were simulated using appropriate mass fractions for each element, shown in Table 10. These amounts differ slightly from the composition of the TEP on CRaTER because the TEP on CRaTER contains a small amount of fluorine (Ref. 27). The FLUKA materials library does not contain fluorine, so the small amount of fluorine was treated as oxygen for the purposes of the

Table 10: Mass fractions of different elements used to simulate TEP

Element	Mass Fraction
O	0.0807
H	0.1033
C	0.7693
N	0.0330
Ca	0.0137

simulation. It is not expected that this substitution will substantially affect the properties of the TEP, as simulated.

For the purposes of comparison with both the experimental data and the build-up using the lookup tables, several sets of scoring detectors were implemented. The first set of detectors used the same depth in the lookup tables. The detectors were identical in location past the zenith shield and in depth. Because this simulation attempts to model CRaTER to a reasonable degree of accuracy, the width of the detector is reduced to that of CRaTER rather than the arbitrarily large width found in the lookup table calculation. These detectors allow for direct comparison with the lookup table locations to examine the differences at the same location. The second set of detectors are set as the same size and shape as the detectors in CRaTER. These detectors are much larger than the slivers set up in the lookup tables but should provide a closer representation of the detectors in CRaTER. These detectors are unable to discern the location of an event within the detectors, so this technique may result in some improved accuracy

H. CRaTER Experimental Data

The CRaTER experimental data has recently become available for analysis and comparison the FLUKA simulations (Ref. 8). Figure 10 shows the CRaTER data as presented by Case, using the same binning structure that is used throughout this paper. These data show the deposition of energy in detectors D1(thin) and D2 (thick), with the triple coincidence criterion applied, requiring that energy be deposited in D2, D4, and D6 (all thick detectors) in order for the event to be counted. As discussed above, these data are derived from the data collected by CRaTER on the LRO for the period from June 29, 2009 to December 31, 2010.

Figure 10 also demonstrates the locations of the ion peaks in the CRaTER data, as identified by Case *et al.* (Ref. 8). The locations of these ion peaks are important to the comparison of the FLUKA lookup tables to CRaTER data because the FLUKA data was calculated by ion, and the relative location and size of the ion peaks is significant in identifying and analyzing how the physics of each ion interaction affects the accuracy of the model. The existence of the CRaTER data, which measured the lineal energy spectrum outside the influence of Earth's magnetosphere provides an excellent opportunity to benchmark the FLUKA lookup tables against experimental data.

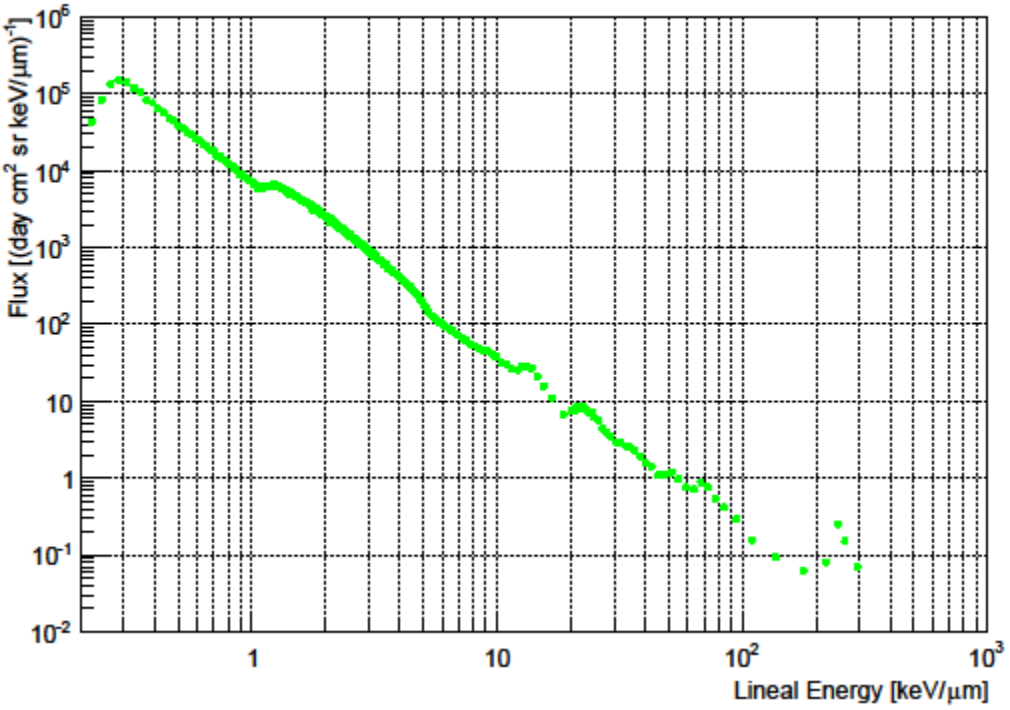

Figure 10: Data obtained from CRaTER Telescope from June 29, 2009 to December 31, 2010 (Ref. 8)

I. CRaTER Model

1. Comparison of Results to Experimental Results

As explained above, the CRaTER data provides an excellent opportunity to benchmark the FLUKA simulations that were conducted in this work and provides a good overall assessment of the technique of using Monte Carlo lookup tables generally. Figure 11 shows the CRaTER experimental data from detectors D1 and D2, binned per the process described by Case *et al.*, compared to the FLUKA lookup table values obtained for this work. Figure 12 displays the same information with a straight line drawn between consecutive data points for ease of viewing.

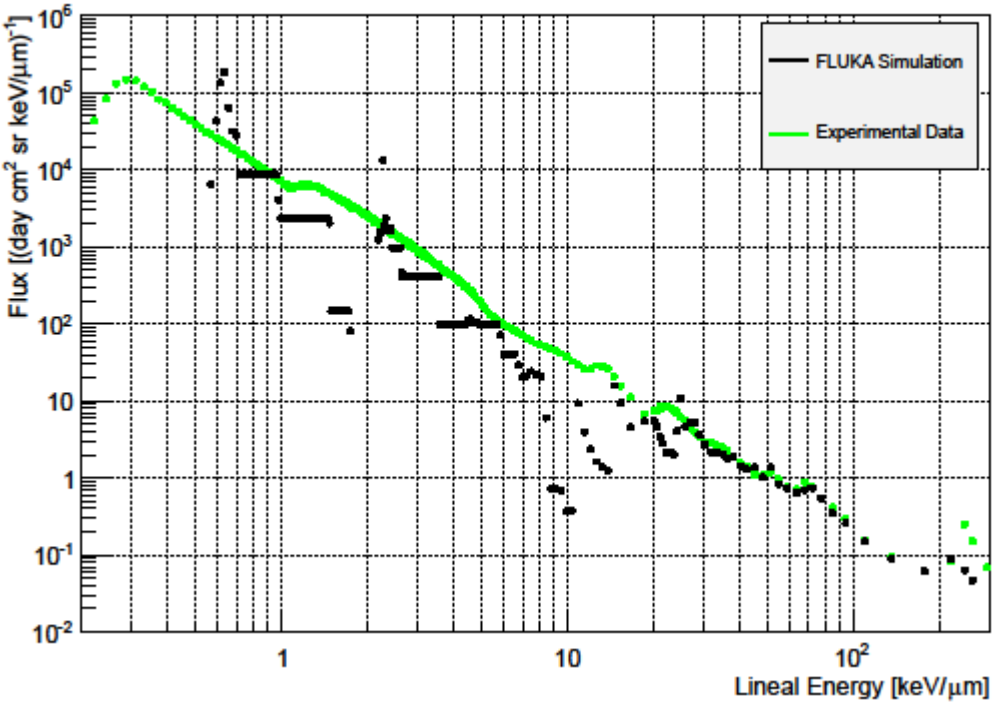

Figure 11: Flux v. Lineal Energy for FLUKA Simulation and CRaTER Experimental Data (Ref. 8).

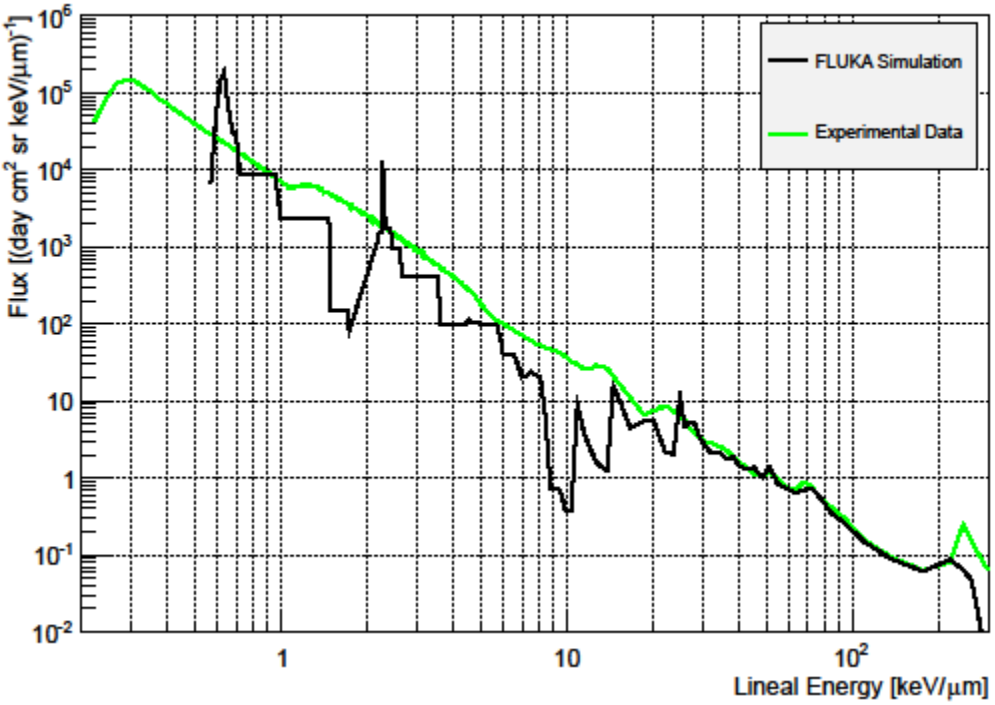

Figure 12: Flux v. Lineal Energy for FLUKA Simulation and CRaTER Experimental Data Shown with Connecting Line (Ref. 8).

An examination of Figure 12 and the calculations for individual ions raises several issues about the distribution of the fluence between the calculated energy and the next lower energy. First, the method of distributing the fluence evenly between neighboring energy points introduces error at points where lineal energy changes rapidly as a function of incident energy. Second, the behavior near the peaks is affected disproportionately by the selection of which depth in the FLUKA lookup tool was used to model the detector. Third, the peaks, especially those at low-Z, exhibit a significant shift to higher lineal energy due to the manner in which lineal energy has been calculated from absorbed dose and the use of average rather than most likely energy deposition as shown by Bischel (Ref. 38). Fourth, there are two gaps in the

CRaTER simulation made using the FLUKA lookup tool, which are likely the result of the choice of incident ions and the selection of incident energies. Fifth, the FLUKA lookup tool simulation exhibits better agreement to the experimental data at higher lineal energies, where a wider variety of incident ions are contributing to the spectrum. These issues are explained in more detail below.

First, the manner in which fluence is distributed among the lineal energies results in inaccuracies where the lineal energy is changing rapidly as a function of incident energy. Silicon ions (Z=14) at the D1/D2 detectors, shown in Figure 13, provide a good illustration of the issue. Between 40 and 60 MeV/n, the calculated lineal energy increases by two orders of magnitude from 1.8 keV/μm to 448.1 keV/μm. The peak lineal energy likely occurs somewhere between 40 and 60 MeV/n, but the location or height of the peak cannot be ascertained on the basis of these data. The algorithm used to produce the CRaTER simulation in Figure 12 distributes the fluence that was calculated for 60 MeV/n using BO'10 (0.1 cm^{-2} sr^{-1} day^{-1}) across this entire lineal energy range. The broadness of the lineal energy range over which the fluence is diluted causes an underestimation of the fluence at the peak lineal energy. As an example, if the maximum lineal energy were located at 50 MeV/n, then the fluence attributed to the 60 MeV/n point should be deposited in a small lineal energy band at a lineal energy higher than the 60 MeV/n datum. The primary impact of this phenomenon is to lower the peak fluence for some ions.

Second, the behavior near the peak is also affected by the selection of detector from the FLUKA simulations to simulate CRaTER. Figure 14 shows the same silicon ions that are

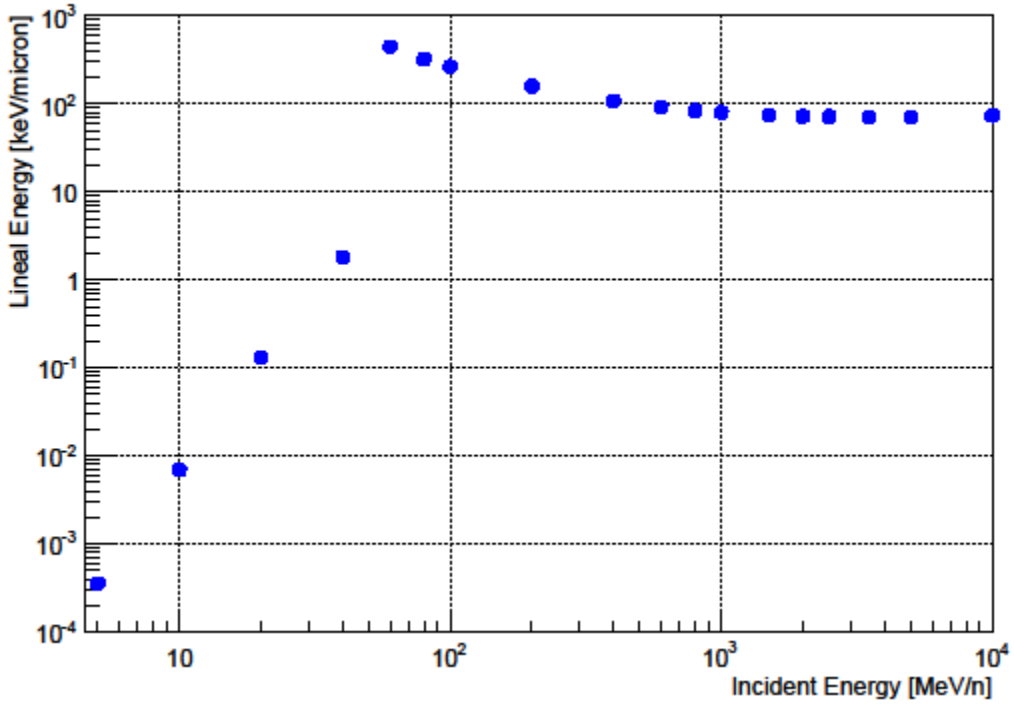

Figure 13: Lineal Energy v. Incident Energy for Silicon Ions at D1/D2.

discussed above, but the lineal energy for the first and last detectors that could be used to simulate D1 and D2 are plotted. These detectors were located at water depth 0 cm and 0.16 cm. Their behavior at high energies, where the ion does not undergo a significant reaction in the target is nearly identical, but the peak lineal energy for the 0.16 cm detector occurs at 60 MeV/n vice 40 MeV/n for the 0 cm detector. Below the peak (i.e., less than 40 MeV/n), the behavior of the curves differs significantly; however, as discussed above, these low lineal-energy depositions do not influence the behavior of the detector because the low-energy particles are not capable of meeting the triple coincidence requirement.

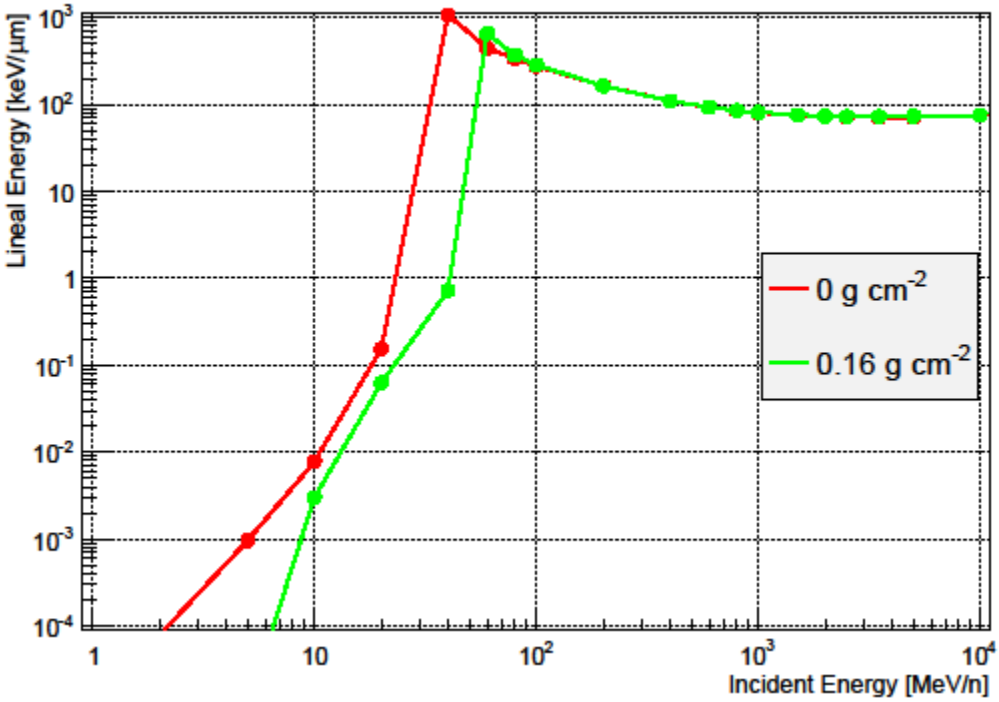

Figure 14: Lineal Energy v. Incident Energy for Silicon Ions near Opposite Ends of the D1/D2 Detectors

Third, significant shifts are observable in the low-Z peaks due to several contributing factors, such as the manner in which lineal energy is calculated and the impact of the Vavilov distribution (Ref. 38). The proton peak for the FLUKA data occurs at 0.64 keV/µm, whereas the experimental proton peak occurs at 0.30 keV/µm. Likewise, the alpha peak appears at 2.28 keV/µm in the calculations, but in the experimental data, the peak is near 1.26 keV/µm.

The calculation of lineal energy from absorbed dose tends to overestimate the point values of the lineal energy because the absorbed dose calculation is, by its nature, an average of the energy deposited in the detector over the histories that generate these results. These averages are skewed to the higher values because rare events such as a collision between the incident ion

and a nucleus deposit large amounts of energy but are relatively rare. A collision might occur only once in several hundred histories, but the energy imparted by the collision may exceed the most common energy loss by several orders of magnitude. In a physical detector, these events would be recorded as two separate peaks at different lineal energies. However, when absorbed dose is used to approximate lineal energy, the two peaks are averaged, resulting in a peak that is higher than the peak that is recorded for the ions by the physical detector. The primary impact of this phenomenon is to shift the peaks calculated using the FLUKA lookup tool to the right.

Fourth, there are a number of locations where no points are plotted because no data points calculated to fall within their boundaries. As described above, it was decided that these points should not be plotted because they are an artifact of the binning choices. Likewise, there are some regions where several consecutive points have been plotted at the same fluence levels. The most notable examples of this behavior occur just above 1 and 3.5 keV/μm. This plot behavior is also a function of the binning choices. Figure 15, shows the proton and alpha calculations plotted against the CRaTER experimental data, demonstrates these two phenomena. The 200 MeV/n proton point is plotted uniformly between 0.98 and 1.49 keV/μm, the calculated lineal energies for 200 and 100 MeV protons respectively. The 100 MeV proton datum is plotted between 1.49 and 1.74 keV/μm, but it contributes a minimal amount of fluence because only one quarter of the fluence (estimating the portion between 95 MeV and 100 MeV) is deemed to contribute. The lineal energy of the alphas is entirely above this range, and no other proton energies contribute. Therefore, the 200 MeV/n proton fluence value is divided evenly among

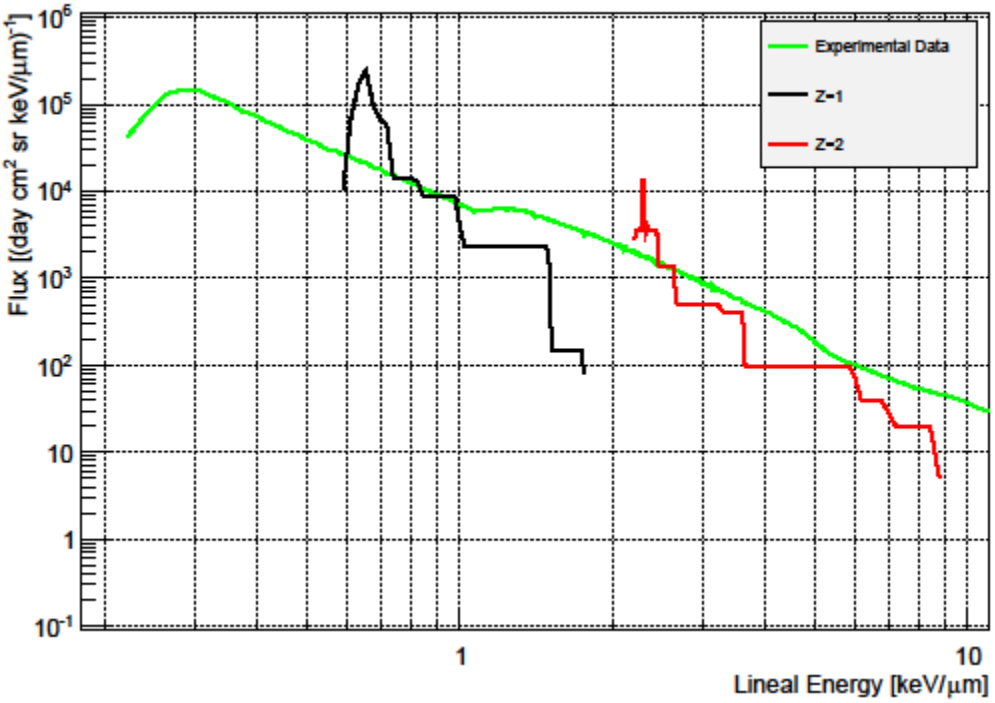

Figure 15: Proton and Alpha Contribution to FLUKA CRaTER Simulation Result

these bins, resulting in a horizontal line. At the high end of the horizontal line, the fluence dips slightly, showing that the 200 MeV/n does not traverse this entire bin. This bin ends at 1.496 keV/µm compared to 1.492 for the 100 MeV/n protons.

Compared to the highest proton lineal energy with non-zero fluence of 1.492 keV/µm, the lowest alpha lineal energy from the FLUKA lookup tool is the 800 MeV/n with a lineal energy of 2.191 keV/µm (near the alpha edge). This difference results in a gap between the proton and alpha peaks for which the FLUKA simulation contains no data. There are several possible explanations for the presence of this gap in the calculations. First, the use of a cutoff energy to duplicate the triple coincidence requirement leads us to discard portions of the spectrum that

would fill in this gap. In reality, this approach discards too many primaries because the primaries with lower energy can deposit energy in the downstream detectors via other particles such as delta rays. Figure 16 shows fluence plotted against incident energy for protons and alphas. The proton lineal energy is less than the lowest alpha lineal energy above 100 MeV/n. The primaries at or below 100 MeV/n for protons are assigned a fluence of 0 to account for triple coincidence. Figure 17 provides a closer view of this region, highlighting the area where the apparent fluence is nil and how the energy cutoff contributes to this characteristic. Second, the FLUKA simulations only reproduced the most common isotope of each ion. Therefore, no calculations were performed using deuterons, tritons, or ^{3}He, all of which could affect the energy deposition in this region. Third, the use of cutoff energies does not account for reactions with threshold energies, so the values that are used over each energy range may not in all cases be representative of the range.

Although the choice of detector location caused observable effects for the high-Z ions, as discussed above, the effect of this choice on the low-Z ions is not as pronounced, primarily as a result of the energy cutoffs. Figure 18 shows a plot of lineal energy versus incident energy for protons at the 0 cm detector and the 0.16 cm detector. Above the energy cutoff, there is little difference between the calculated lineal energies. Therefore, it is not expected that the choice of FLUKA detector location to simulate D1 and D2 had a significant impact in this portion of the lineal energy spectrum.

Fifth, above 20 keV/μm, there appears to be better agreement between the FLUKA simulation results and the experimental data, and the plot appears to be smoother. Figure 19

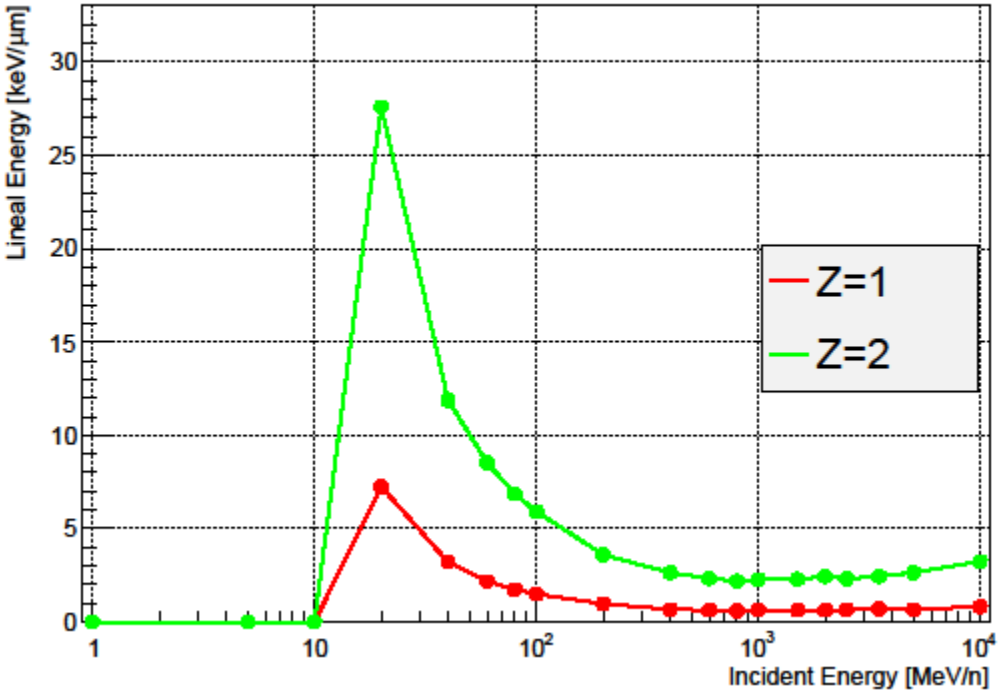

Figure 16: Lineal Energy v. Incident Energy in D1/D2 for Protons and Alphas.

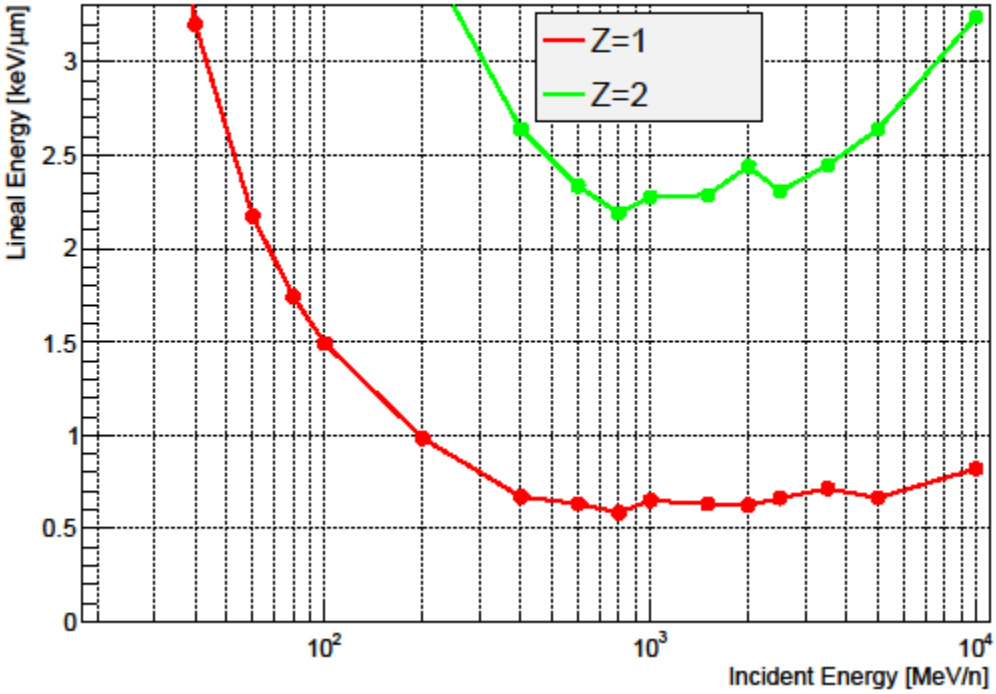

Figure 17: Lineal Energy v. Incident Energy in D1/D2 for Protons and Alphas Illustrating the Gap Region.

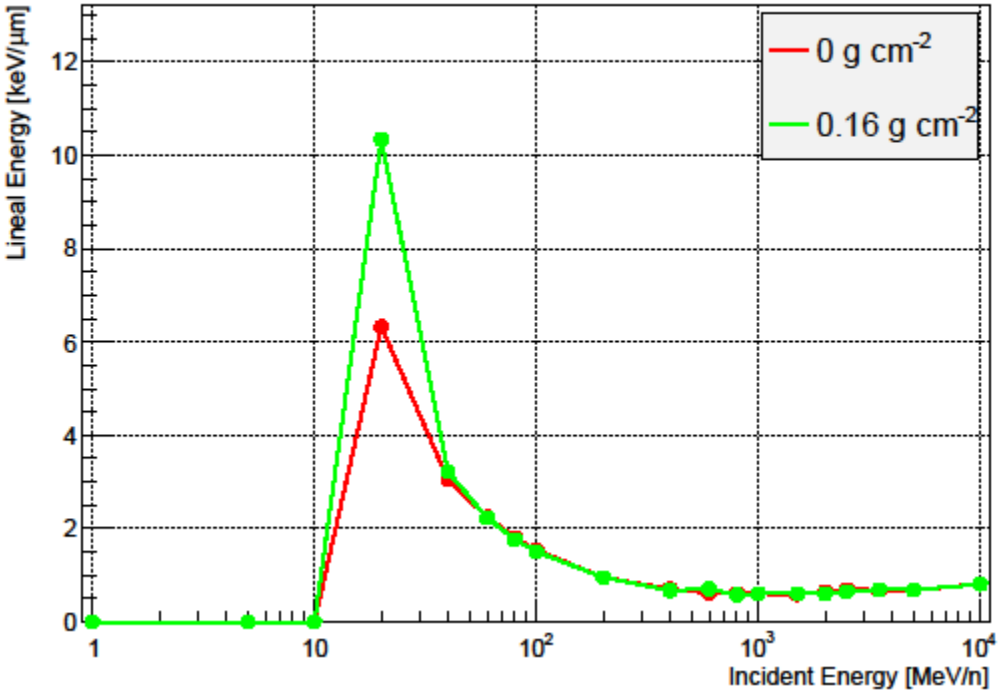

Figure 18: Comparison of Detectors at 0 g cm^{-2} and 0.16 g cm^{-2} for Incident Protons.

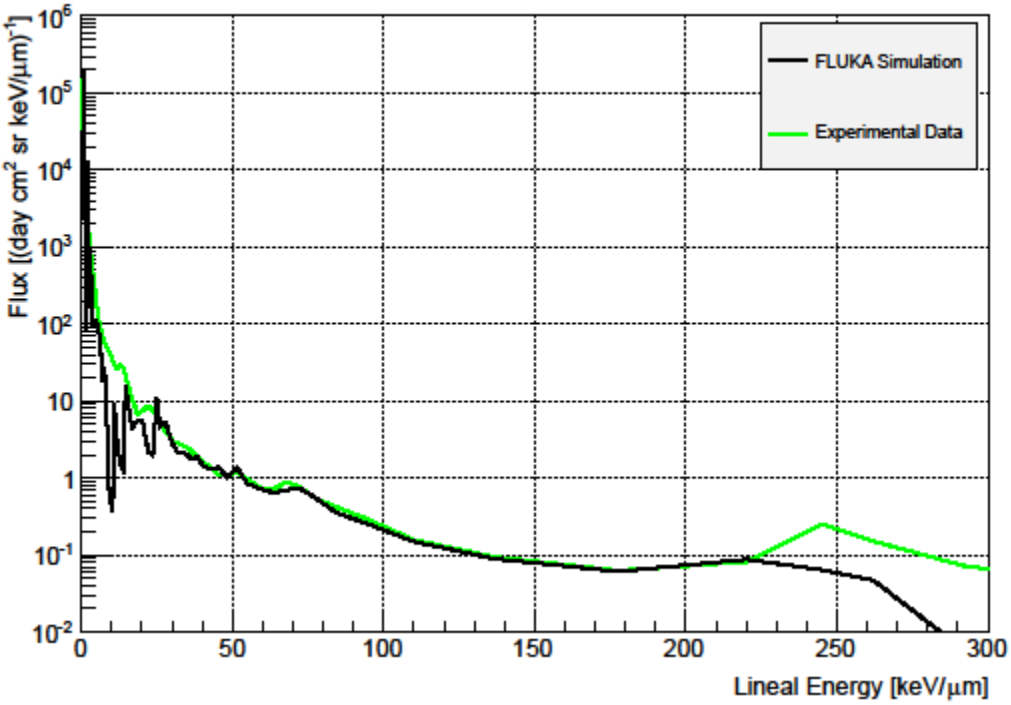

Figure 19: FLUKA Simulation and Experimental Data Plotted on Linear Energy Axis (Ref. 8).

shows the FLUKA calculations against the experimental data with the lineal energy plotted on a linear axis. This plot demonstrates that the logarithmic plot is not masking variability at the higher lineal energies. However, the plot demonstrates less agreement at lineal energies above 200 keV/μm, near the iron peak.

The increased smoothness at higher lineal energies likely result primarily from the higher concentration of ions with characteristic energy depositions at higher lineal energies. As a result of the higher concentration, the data points are the result of the interactions of several ions, so simulation choices such as energy cutoffs do not have as significant an impact. Even if one ion's

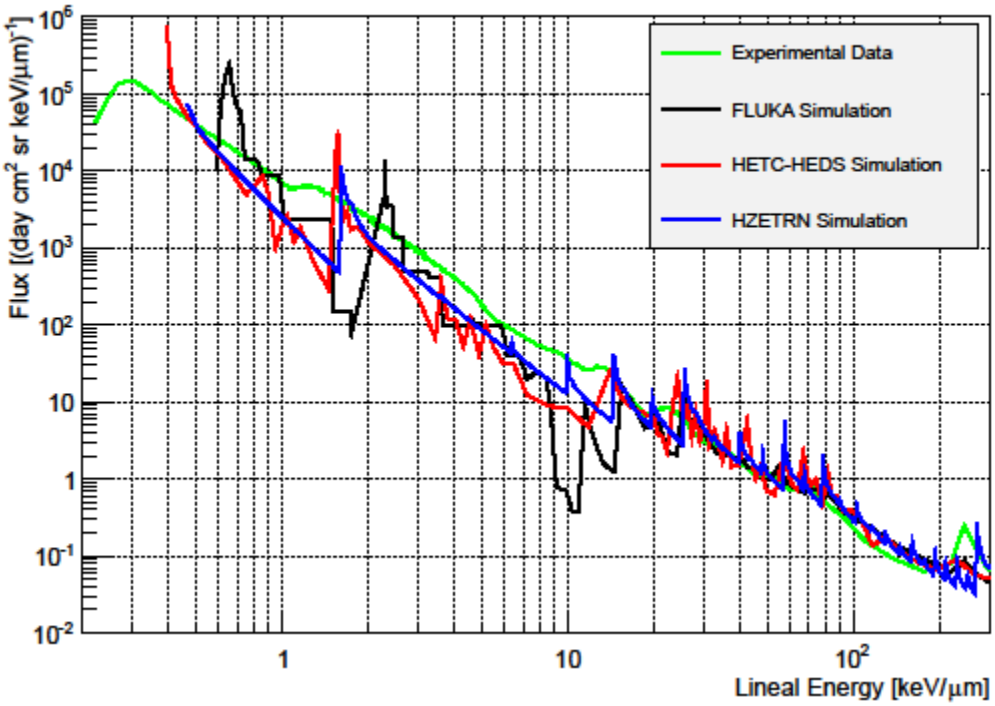

Figure 20: FLUKA, HETC-HED, and HZETRN Simulations Plotted Against CRaTER Experimental Data (Refs. 8, 21, 42).

contribution is truncated, several other ions are also contributing, which conceals the effect of the calculation choices made for each individual ion.

2. Comparison to Other Codes

Other codes have been used to simulate the CRaTER detector with similar results (Ref. 21, 42). Figure 20 shows CRaTER simulations produced using HZETRN and HETC-HEDS and the results developed with the FLUKA lookup tables compared to the experimental data (Ref. 8, 42). HZETRN and HETC-HEDS invoke different models of the physics of charged particles

interactions, so it is significant that the models are in relative agreement with each other and the CRaTER data. Several features of these simulations are notable.

First, the other simulations exhibit a similar peak shift due to the Vavilov correction, but the magnitude of this correction is not as great as it is for the FLUKA lookup tables. The proton peak for the HETC-HEDS simulation occurs at about 0.39 keV/μm, which is the value one obtains from the Bethe-Bloch equation. It appears that the HZETRN peak will be located at 0.47 keV/μm. The FLUKA lookup table simulation calculates the proton peak at 0.64 keV/μm, which is significantly higher than the other simulations. Likewise, the alpha peak appears at 1.60 and 1.61 keV/μm for HETC-HEDS and HZETRN respectively. The FLUKA lookup table peak appears at 2.34 keV/μm. This difference appears to result from the difference in detector thicknesses used for each simulation. The HETC-HEDS detectors are simulated as being the same size as the detectors in the CRaTER instrument, but the FLUKA lookup tables used detectors that are 1 μm in depth. The HZETRN simulation calculates the point value of the quantity because HZETRN is a deterministic code. Therefore, the FLUKA lookup table detectors should be expected to show a much greater difference as a result of the difference resulting from the Vavilov distribution.

Second, with respect to the two points for the FLUKA lookup tables where the curves significantly underestimated the data, it appears that the HETC-HEDS and HZETRN simulations also underestimate the experimental data near 1 and 10 keV/μm. This similarity is remarkable because of the differences in physical models used to simulate the detector among the three different Monte Carlo codes. This similarity indicates that it is likely that the conditions imposed

on the simulations for triple coincidence are a primary contributor to this gap. The low lineal energy near the first gap indicates that the gap must result almost entirely from the energy deposition of incident protons. The selection of incident energies does not appear to be a contributor. Whereas the FLUKA lookup tables calculate no energies between 100 MeV and 200 MeV, the HETC-HEDS simulation calculate incident energies every 10 MeV between 100 and 200 MeV. Furthermore, HZETRN does not calculate for discrete incident energies, treating incident energies as continuous. Therefore, it is unlikely that the choice of incident energies contributed significantly to the underestimation in this region for the HZETRN calculations. The FLUKA ion calculations show that at approximately 10 keV/μm, the behavior of the alpha and boron energy depositions are the primary contributors to the drop. Figure 21 shows a more detailed depiction of the behavior of the energy deposition in this area. In the FLUKA lookup table result, the first gap results from the end of the alpha particle contribution. The boron peak then causes the overall energy deposition to rise briefly, and the overall peak decreases to an order of magnitude less than the experimental data as the boron contribution decreases.

The triple coincidence requirement is not entirely responsible for the underestimation in these regions. As Figure 22 illustrates, dispensing with the energy cutoff in the FLUKA simulation ameliorates this situation, primarily due to the extension of the upper range of the proton and alpha energy deposition. Although this approach eliminates the data gap between protons and alphas, it does not eliminate the underestimation in these regions, and the existence of this underestimation in the calculations using FLUKA, HETC-HEDS, and HZETRN suggests that the underestimation results from a common factor other than the energy cutoffs. The

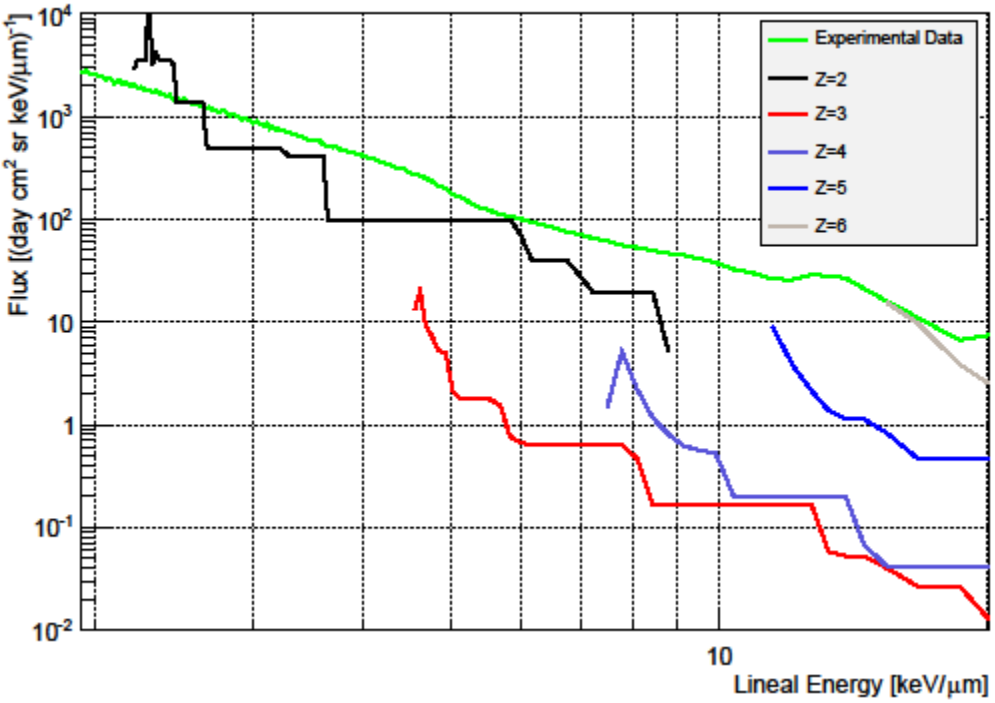

Figure 21: Ions Contributing to the Underestimation of Experimental Data near 10 keV/µm.

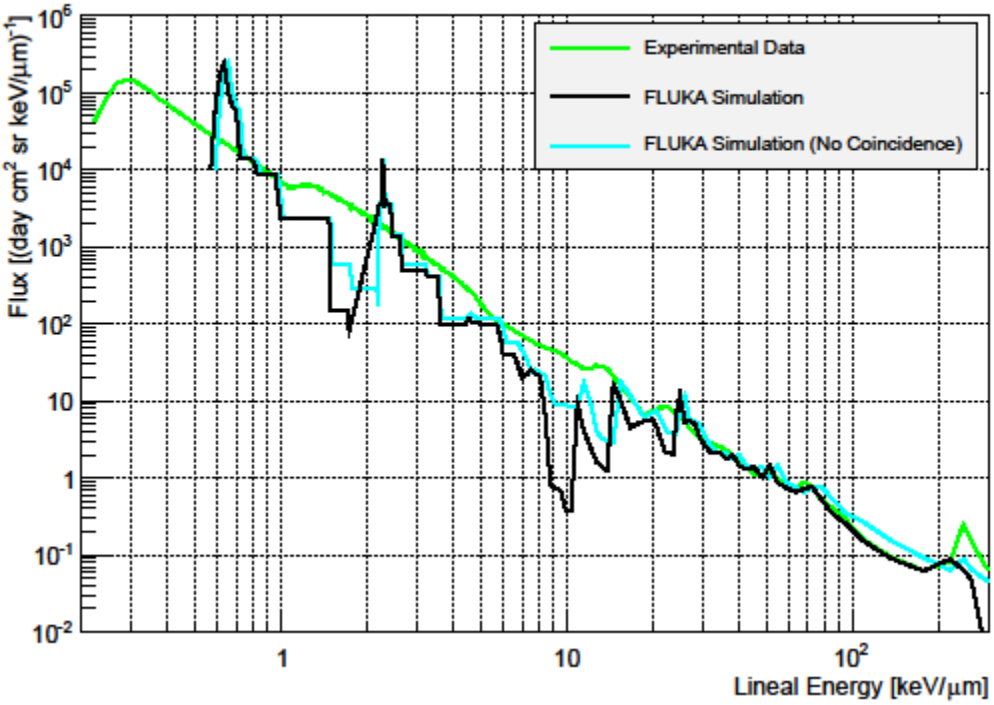

Figure 22: FLUKA Simulation Plotted against Experimental Data with and without Triple Coincidence Requirement (Ref. 8).

calculations made using these codes treat delta ray transport differently. FLUKA transports the delta rays above an energy threshold, the HETC-HEDS simulation applies a delta ray correction formula, and HZETRN treats delta ray energy as deposited locally (Ref. 21). Other possible explanations include the presence of unsimulated ions such as deuterons, tritons, and ^{3}He in the GCR spectrum, a difference in the GCR spectrum incident on CRaTER from the BO'10 code approximation, or three-dimensional effects resulting from the fact that the simulations all treat the ions as incident along the detector axis.

Overall, these three simulations display remarkable similarity in their simulation of the CRaTER detector, given that energy deposition was calculated using different physical models in

each case. The ability of the FLUKA lookup tables to replicate the results of more accurate simulations that take the specific geometry of CRaTER into account tends to show that the use of lookup tables for quick calculations of the GCR spectrum are viable.

3. Comparison of FLUKA Lookup Table Result to FLUKA with direct modeling of CRaTER

As explained above, a comparison between a model more closely following CRaTER's geometry and at a larger number of energies provides the ability to examine the efficacy of the lookup table, separate and distinct from the ability of FLUKA to model the CRaTER telescope. Figure 23 and Figure 24 show a plot of the BO'10 fluence versus calculated lineal energy from dose data. Figure 23 shows the points as they are plotted, and Figure 24 shows the same information connected by a simple line for ease of viewing.

Several features of the direct model are notable. First, as with the lookup table calculations, the ion peaks appear to be shifted to the right. This characteristic is particularly apparent in the proton and alpha peaks. The proton peak, which appears at 0.3 keV/μm in the experimental data is located at 0.45 keV/μm in the CRaTER simulation. Similarly, there is a notable shift in the alpha peak from 1.26 keV/μm in the experimental data to between 1.75 and 1.90 keV/μm in the CRaTER simulation. Porter's HETC-HEDS calculation of the proton and alpha peaks place the peaks at 0.39 and 1.55 keV/μm respectively (Ref. 42). Therefore, the peaks in the FLUKA CRaTER simulation are more significant than the peak shifts reported by Porter.

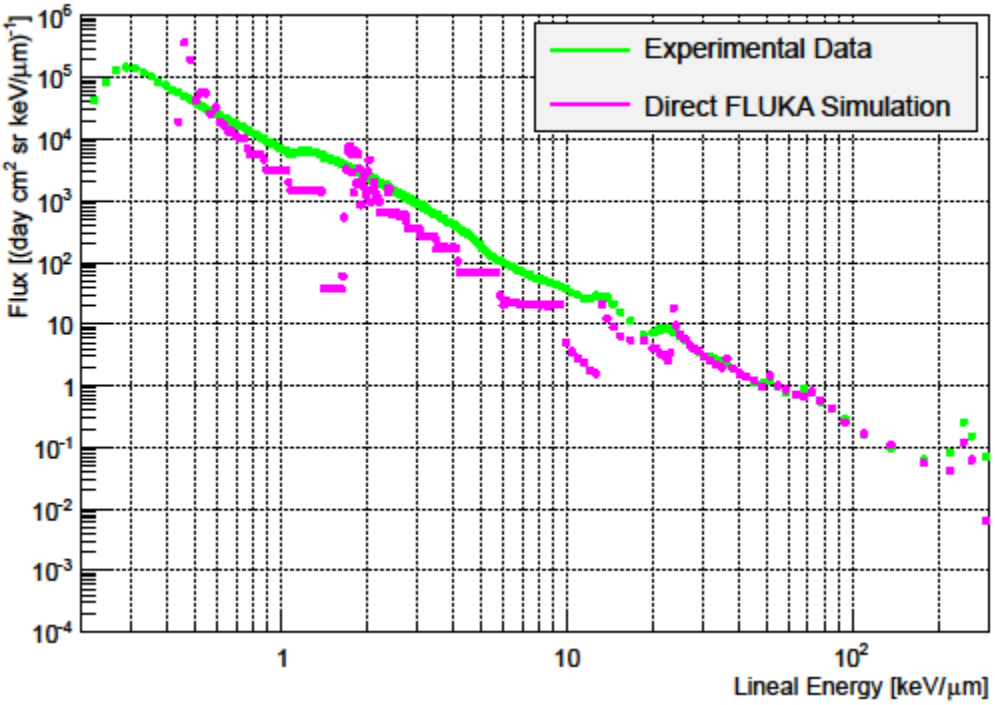

Figure 23: Direct Simulation of CRaTER Using FLUKA Compared to the Experimental Data.

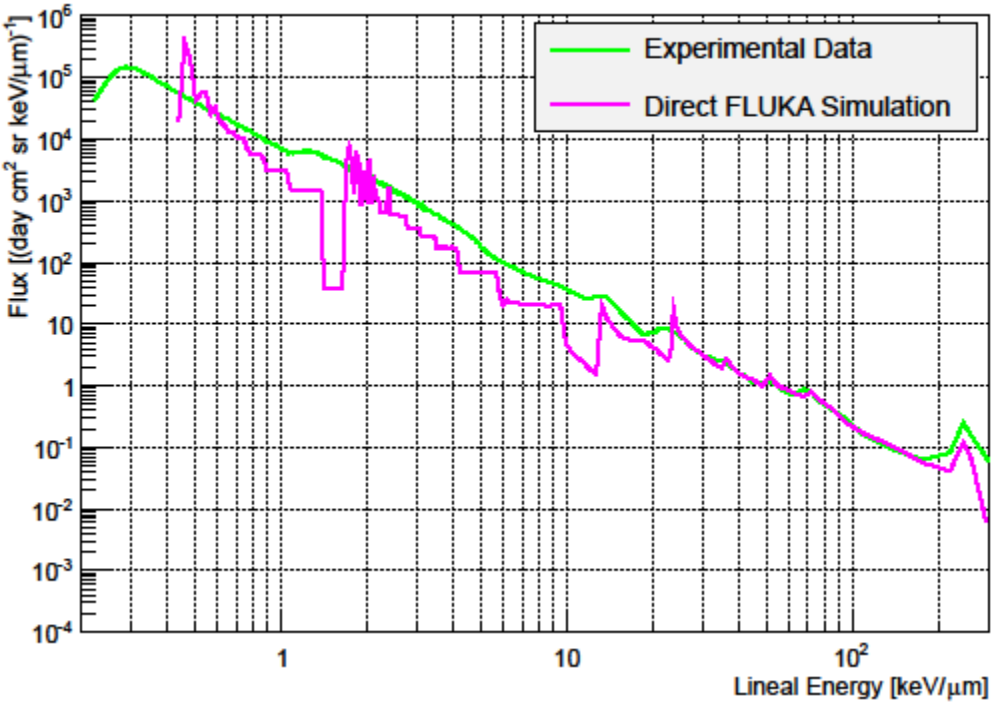

Figure 24: Direct Simulation of CRaTER Using FLUKA Compared to the Experimental Data Connected with Simple Lines.

However, the peak shifts in the CRaTER simulation are not as large as those calculated using the FLUKA lookup tables. Figure 25 and Figure 26 show the CRaTER simulation and the FLUKA lookup table simulation of CRaTER plotted against the CRaTER experimental data. Figure 25 displays the calculated points, and Figure 26 shows the points connected by a simple line for ease of viewing. As expected, the direct CRaTER simulation exhibits less peak shift. This difference results from the simulation of the detectors using the actual detector sizes (148 and 1000 μm) rather than the 1 μm detectors used to develop the FLUKA lookup tables. Because the Bischel effect becomes more severe as the detector becomes thinner, it is expected

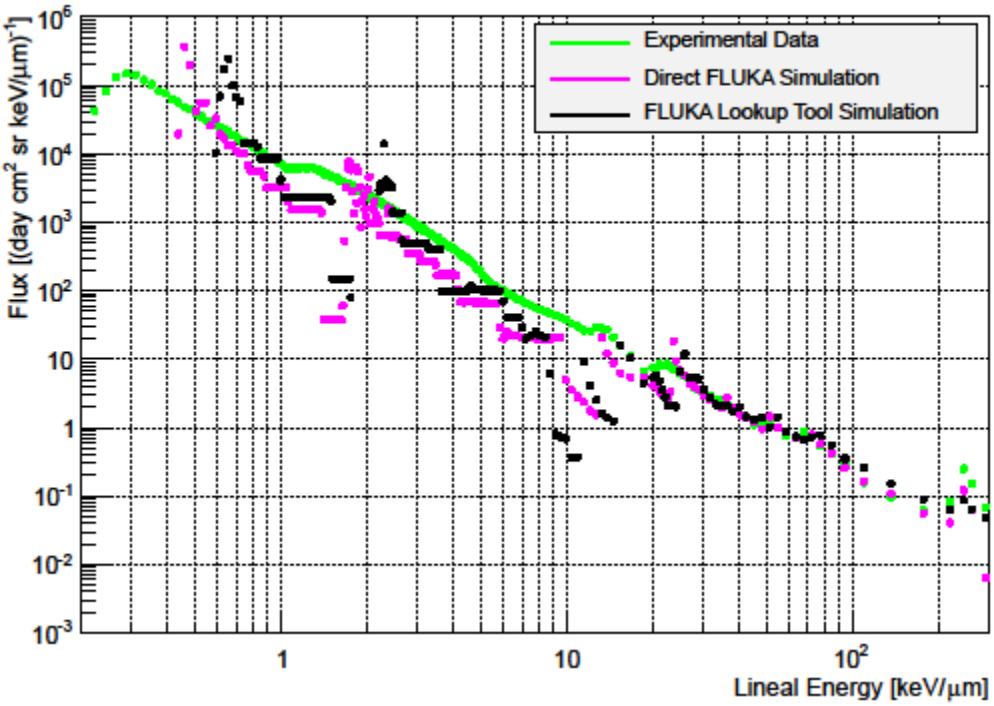

Figure 25: Comparison of calculations of D1/D2 in the CRaTER Telescope by Direct Modeling and the FLUKA Lookup Tool to the Experimental Data.

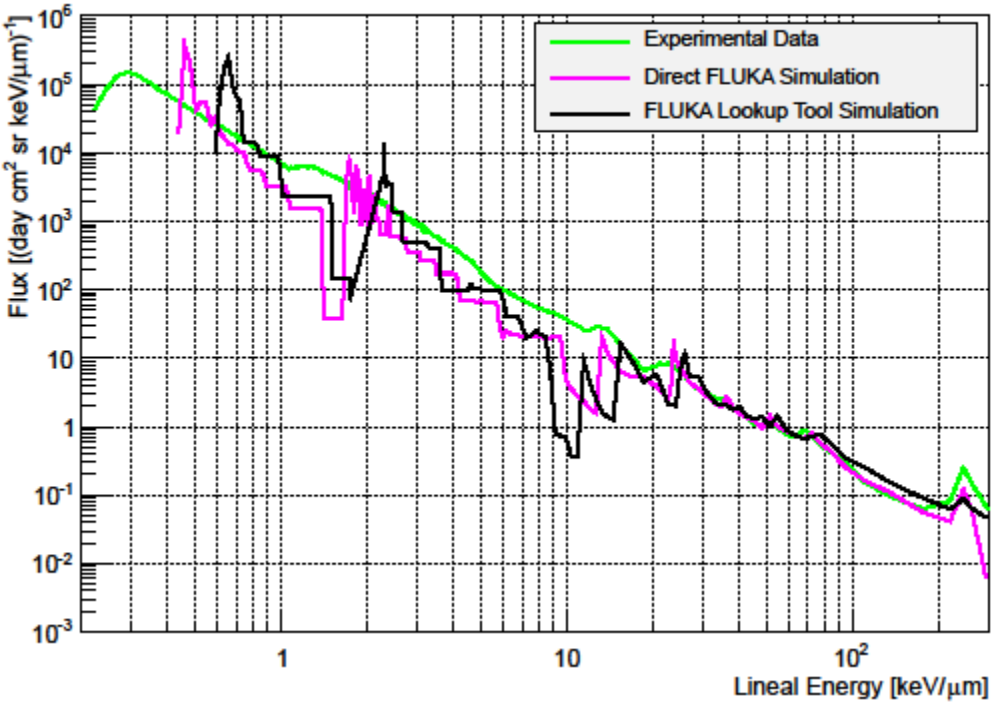

Figure 26: Comparison of calculations of D1/D2 in the CRaTER Telescope by Direct Modeling and the FLUKA Lookup Tool to the Experimental Data Connected by Simple Lines.

that the peaks in the direct CRaTER simulation, which are thicker, would be closer to the experimental data.

An examination of the ion peaks for the CRaTER simulation shows that the direct simulation improves, but does not eliminate, the characteristics of the FLUKA lookup tables where the fit with the experimental data is the least good. Figure 27 shows the lineal energy by ion, plotted with the CRaTER experimental data. Although the CRaTER simulation eliminates the data gap between the proton and alpha peaks that is present in the FLUKA lookup tables, the CRaTER simulation still underestimates the experimental data by approximately one order of

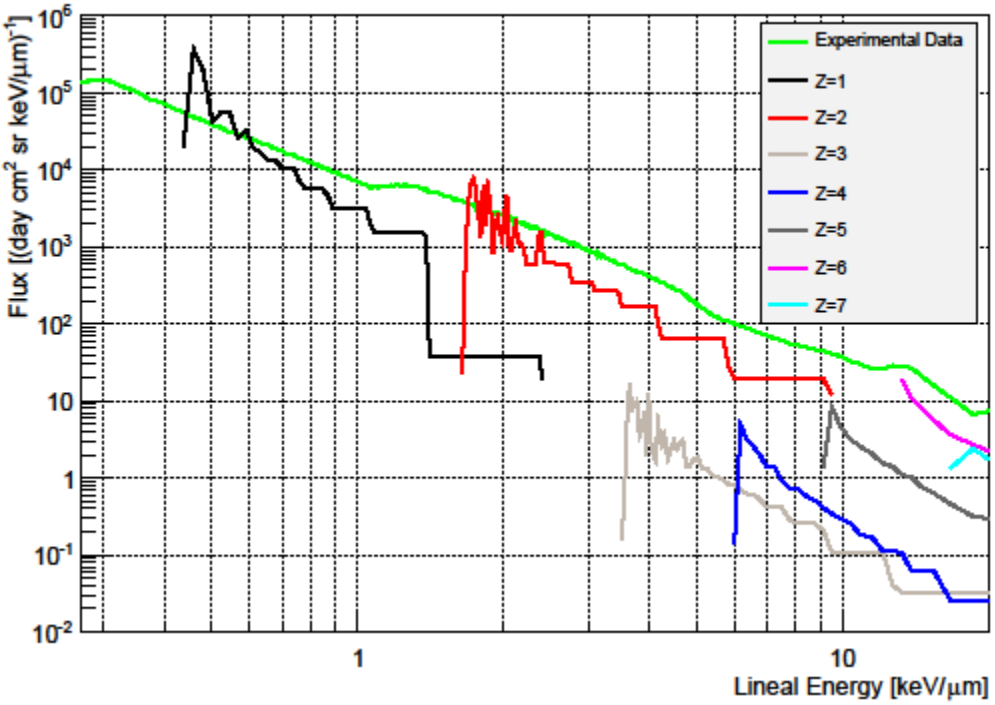

Figure 27: Ion Contributions to Direct Model of CRaTER Telescope for D2.

magnitude between the proton and alpha peaks. Because the Bischel shift is greater in absolute magnitude for higher Z particles, it appears that the Bischel shift is responsible for this gap at least in part. As discussed earlier, it is also possible that factors such as the artificiality of the energy cutoffs or the non-simulation of particles such as deuterons, tritons, and ^{3}He contribute to the simulation's behavior at this point, where the characteristic energy depositions of the individual ions do not overlap as much as they do at higher lineal energies.

In other respects, it appears that the direct simulation of the CRaTER detector produces better results than the use of lookup tables. However, the results obtained using the lookup tables are comparable to those obtained with direct modeling using FLUKA as well as the other codes. Based on a comparison between the FLUKA lookup tables and the direct simulation, the

most significant differences appear to stem from the difference in the Bischel shift due to the detector thickness and the absence of a data gap in the direct simulation. At the two points where the simulations significantly underestimate the fluence, the direct CRaTER simulation performs better but does not eliminate the underestimation.

VI. Effective Dose Analysis for Shielding Configurations

A. Calculation of Effective Dose and Comparison to NASA PELs

As described above, it is hoped that the lookup table calculations assist NASA reach its goal of reducing exposure to astronauts on long-term missions by 20-30% (Ref. 2). A manned mission to Mars is expected to last 600-900 days, and would result in an effective dose of approximately three to five times the PEL in the current state of technology. In developing the technology for a manned flight to Mars, NASA must balance the radiation reduction benefit of the shielding techniques that it will employ in the spacecraft against the added volume and weight to the spacecraft.

NASA has established PELs for the "primary functions of preventing in-flight risks that would jeopardize mission success, and limiting chronic risks to acceptable levels based on legal, ethical or moral, and financial considerations." (Ref. 43). NASA's newest PELs are mission-specific and limit an astronaut's risk of exposure-induced death ("REID") to 3% using a 95% confidence interval. The PELs take into account the age and gender of the astronaut to determine what effective dose would result in a 3% REID. As an example, Table 11 shows NASA's current PELs for never-smokers for a one year mission.

NASA's PELs are based primarily upon the effective dose to the astronaut. As described above, the NCRP has recommended that NASA use organ dose equivalent rather than equivalent dose to calculate effective dose for the purposes of space missions both within and outside of LEO. The organ dose equivalent is calculated by integrating the dose equivalent over the organ in question. Typically, the organ dose equivalent is calculated by sampling various points within

Table 11: NASA PELs for Never Smokers (Refs. 44 and 45)

	Effective Dose (cSv)	
Age (y)	Female	Male
30	60	78
40	72	88
50	82	100
60	98	117

the organ that are representative of the dose equivalent to the organ. These different points account for differences in shielding resulting from other tissue as well as self-shielding by the organ (Ref. 46).

This work examines the impact of the combinations aluminum and polyethylene shielding developed in the FLUKA lookup tool to limit the effective dose to an astronaut. In addition to the effects of these shielding materials, active shielding methods are also considered. Active shielding methods include the use of electromagnetic fields or plasmas in order to deflect or stop incident charged particles. The use of active shielding methods has been explored since the 1960s as a possible means to provide adequate protection against incident radiation while lowering the weight of the spacecraft or shelter. The methods include electrostatic fields, plasma shielding, confined magnetic fields, and unconfined magnetic fields (Ref. 47).

Townsend has examined the effectiveness of these active shielding methods against the GCR spectrum (Ref. 47). His examination concluded that, while unconfined magnetic fields warranted additional study, that the active shielding methods described above were either ineffective against the GCR spectrum or would not reduce the weight of a spacecraft when compared to material shielding. Electrostatic field shielding is not practical because protection

against the high-energy portion of the GCR would require the creation of potentials that significantly exceed the current state of technology and would be too large for use aboard a spacecraft. Electric potentials greater than 10 GV would be needed to effectively shield 1 GeV/n incident radiation (Ref. 48). Similarly, plasma shields rely upon the creation of an electrostatic field and are not a practical means of protection against GCR. Confined magnetic fields, which consist of a magnetic field that is generated in a specified volume surrounding or within the spacecraft, are similarly not effective against GCR at practical magnetic field strengths (Refs. 47 and 48). Unconfined magnetic fields can be generated by creating a magnetic dipole around the spacecraft or shelter, much like Earth's magnetic poles. Townsend concludes that unconfined magnetic fields "warrant further investigation" because the Earth's magnetic field proves that unconfined magnetic fields can provide effective shielding against GCR. However, a practical and weight-effective unconfined magnetic shield has not been proposed (Ref. 47).

This work provides a rudimentary analysis of the shielding efficacy of confined and unconfined magnetic fields. These active shielding methods can be simulated by simply removing lower energy portions of the GCR spectrum to simulate their inability to penetrate the magnetic field surrounding the spacecraft. It is assumed that the magnetic field will sweep all of the charged particles below a threshold energy around the spacecraft and that the higher energy portions of the GCR spectrum will penetrate the spacecraft with relatively little loss of energy. Although these assumptions ignore the fact that a change to the direction of the incident radiation may be significant based on the shielding geometry, this assumption allows for a simple analysis

of how what portions of the GCR spectrum the active shield would have to protect against in order to be effective when compared to material shields.

The calculations in the FLUKA lookup tool simulate free space that is outside the magnetic influence of a planet. Therefore, they can be used to estimate the effective dose to an astronaut during the transit period of a manned mission to Mars. The effective dose to an astronaut during the transit to Mars has been estimated to be on the order of 1 Sv (Ref. 43). Recently, a measurement of the exposure during the transit to Mars was made by the Radiation Assessment Detector ("RAD") aboard the spacecraft carrying the Mars Science Laboratory spacecraft ("MSL") (Curiosity Rover) to Mars. The RAD provides a good estimate of the exposure expected during the transit to Mars with a few caveats. First, the shielding around the RAD varied between <10 g cm^{-2} to approximately 80 g cm^{-2}, and it is likely that the shielding for a manned mission would differ to some extent. Second, several SPE occurred during the transit, and it is impossible to say whether the SPEs that occurred during the MSL's transit are representative of those that would be encountered during a future manned mission. Assuming that a manned mission to Mars would have similar shielding and GCR environments, Zeitlin calculated that a 360-day transit time would result in a dose equivalent of 662 ± 108 mSv from the GCR alone, with additional exposure resulting from SPE (Ref. 49).

Reducing the exposure of astronauts to GCR during spaceflight will have a significant impact on the overall dose received by the astronauts during long-term flights such as a manned mission to Mars. GCR is always present and is a substantial contributor to the dose received by astronauts during space flight. An examination of the effectiveness of various active and passive

shielding combinations made using the FLUKA lookup tool will provide an efficient means to compare the relative effectiveness of different shielding combinations.

B. Development of Effective Dose Calculations

As explained above, the NASA PELs are expressed in terms of effective dose. Therefore, in order to compare the values calculated in the FLUKA lookup tables for a given GCR spectrum to the PELs, it is necessary to devise a means to calculate effective dose from absorbed dose and dose equivalent in depths of water behind the shielding configurations used to calculate the FLUKA lookup tables. Using water as a proxy for human tissue, the dose and dose equivalent to the relevant organs can be calculated and then be used to develop the effective dose. As mentioned above, for space applications, the NCRP has approved the use of dose equivalent rather than equivalent dose for calculating effective dose (Ref. 46). Therefore, it remains to use the lookup tables and the dose calculations at the available depths of water to estimate the dose and dose equivalent to the relevant organs.

Townsend *et al.* have developed a ray trace program that takes the dose and dose equivalent in a water target and calculates the dose and dose equivalent to all of the organs that are relevant to the effective dose calculation (Ref. 44). This program determined the relevant depths for each organ based on the Computerized Anatomical Man ("CAM") and Computerized Anatomical Female ("CAF") models (Refs. 50 and 51). This program interpolates the relevant depths for the organs based on the available depths in the water target, so the depths calculated in the FLUKA lookup tables were able to be used without modification. Only minor modifications

to the program were necessary to calculate the requisite doses and dose equivalents. Because Townsend *et al.*'s research concentrates on the radiation environment near the Martian surface, it was necessary to remove the assumption that half of the incident radiation spectrum was shielded by the plant because the present calculations address the radiation environment in free space. Therefore, this work assumes no planetary shielding whatsoever. Townsend *et al.*'s research concentrated on SPE spectra rather than GCR spectra, but the ray trace program is equally applicable to GCR because the program allows for the calculation of dose and dose equivalent of various depths and is therefore independent of particle identity.

The dose and dose equivalent resulting from all particles based on their contribution to the GCR spectrum is calculated as described above for the CRaTER detector. The calculated energy deposition data used for the analysis in this case is the same spectrum that existed for the period of the CRaTER data described above. This spectrum was selected for consistency with the other data presented in this work. Obviously, the calculations could be carried out for any other spectrum that the user desires within the limits of the data available from the lookup table.

C. Results of Effective Dose Calculations

The broad range of shielding materials used to create these effective dose calculations gives the calculations the ability to provide an easy assessment of the relative merit of different shielding configurations to a typical GCR spectrum. As detailed above, the same spectrum that provides the basis for the CRaTER data was used to make these effective dose calculations. Figure 28 shows the effective dose per year based on exposure to this spectrum. The different

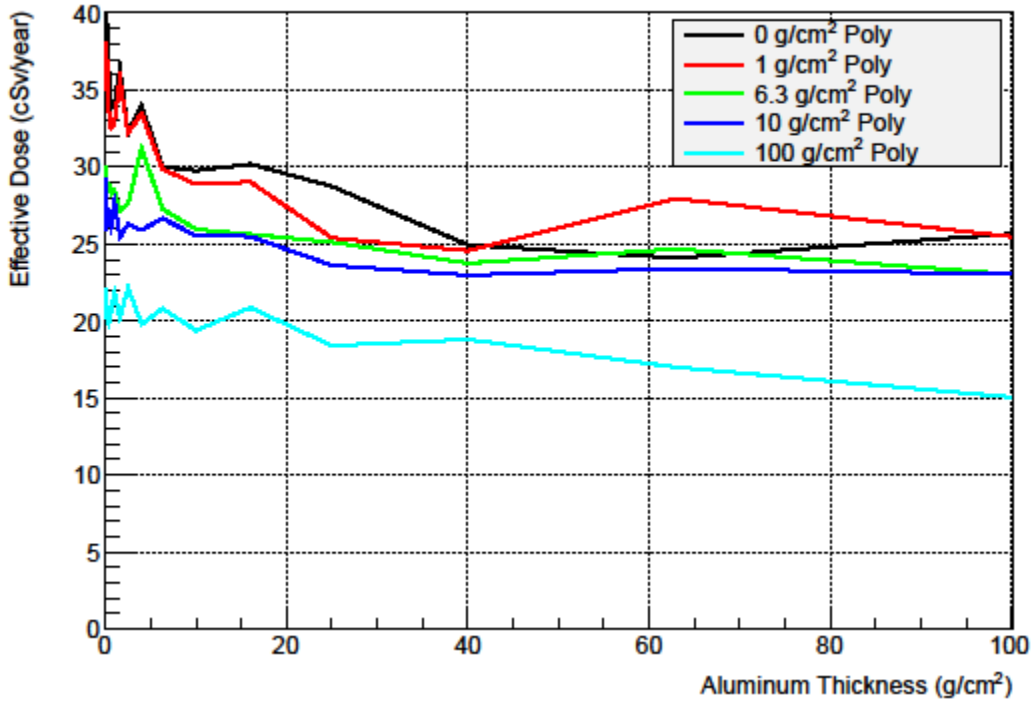

Figure 28: Effective Dose v. Aluminum Thickness for Various Thicknesses of Polyethylene.

lines represent various thicknesses of polyethylene (0, 1, 6.3, 10, 100 g cm^{-2}) that is located immediately behind the aluminum shield. When only a small amount of polyethylene shielding is present, it appears that additional aluminum shielding reduces the effective dose between 0 and 40 g cm^{-2}. Beyond 40 g cm^{-2}, adding aluminum shielding appears to either provide no additional benefit or in some cases exacerbate the effective dose for all but the thickest (100 g cm^{-2} polyethylene configuration. This outcome likely follows from the production of secondary particles in the aluminum shield by high-energy incident particles. Fragmentation within the aluminum then results in less energetic and smaller secondary particles, which then cause greater biological damage. For 100 g cm^{-2} of polyethylene, there is sufficient shielding behind the

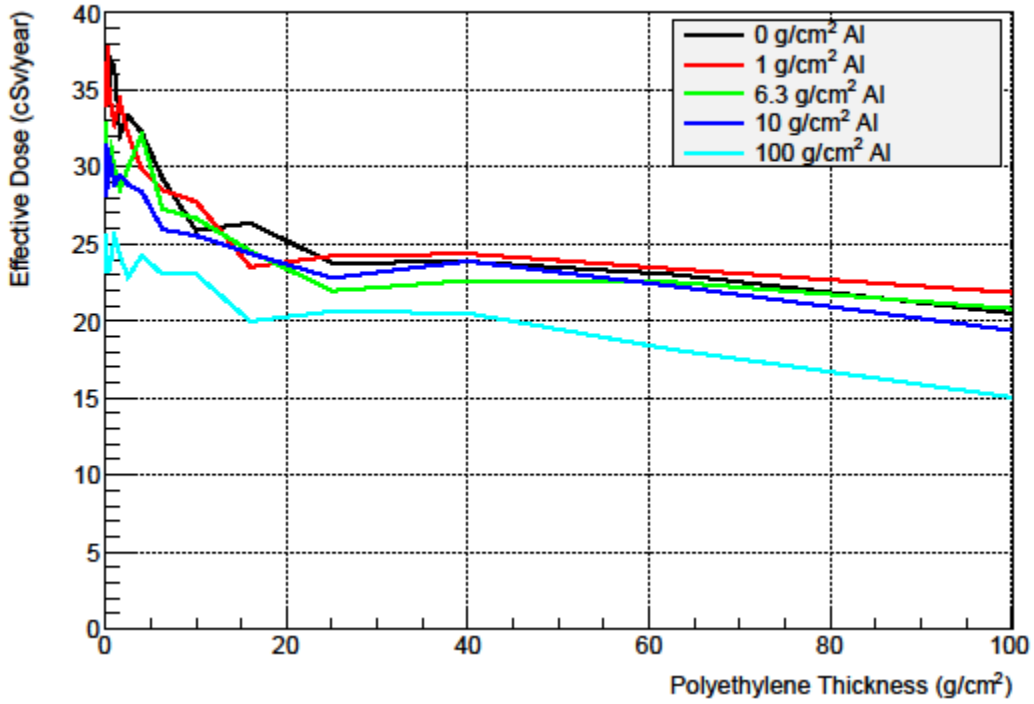

Figure 29: Effective Dose v. Polyethylene Thickness for Various Thicknesses of Aluminum.

aluminum to limit the effect of these secondary ions. Therefore, additional aluminum results in a net benefit; however, the benefit is small. The final 75 g cm^{-2} of aluminum reduces the effective dose by only about 4 cSv/year, which approximately equals the effective dose reduction of the first 25 g cm^{-2} of aluminum.

Figure 29 shows the calculated expected dose per year as a function of polyethylene thickness. The different lines represent 0, 1, 6.3, 10, and 100 g cm^{-2} of aluminum shielding in front of the polyethylene. The addition of polyethylene shielding appears to yield large benefits for all aluminum thicknesses below 16 g cm^{-2}. Although it appears that additional polyethylene

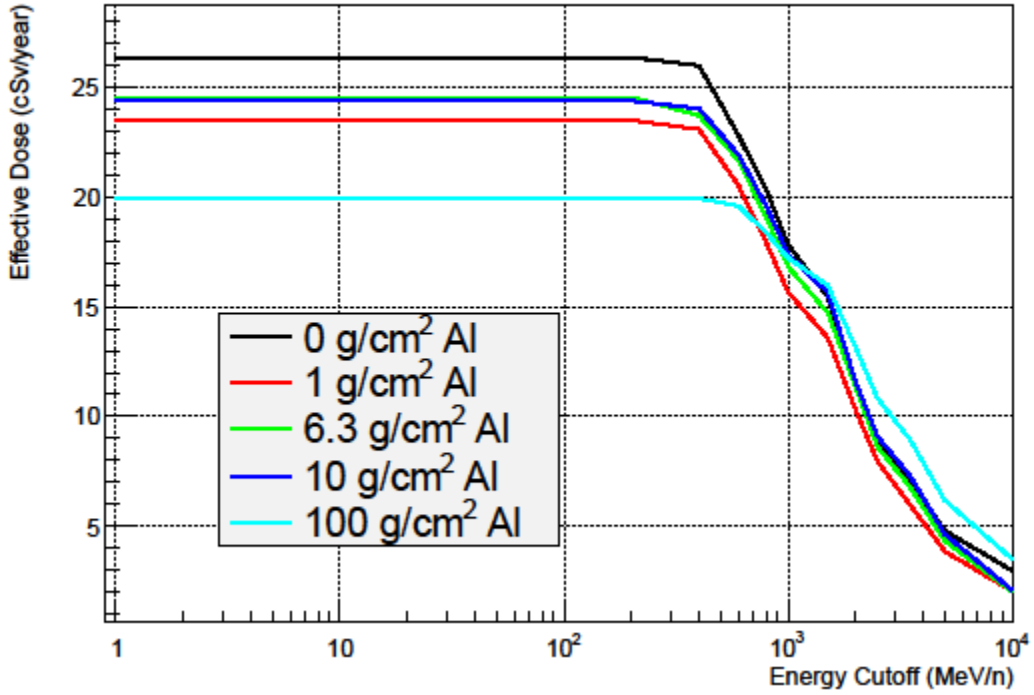

Figure 30: Effective Dose v. Cutoff Energy for Various Thicknesses of Aluminum Shielding Followed by 16 g cm^{-2} of Polyethylene.

will reduce the effective dose further, the incremental benefit for the remaining 84 g cm^{-2} of polyethylene in these calculations is much smaller. For example, with 6.3 g cm^{-2} of aluminum shielding, the effective dose with no polyethylene is almost 33 cSv/year. The first 16 g cm^{-2} of polyethylene reduces the effective dose to 25 cSv/year. At 100 g cm^{-2}, the dose is further reduced to about 21cSv/year. Therefore, the first 16 g cm^{-2} appear to provide 75% of the benefit.

Figure 30 examines the impact of EM shielding on the calculation of effective dose during one year in free space, showing the effective dose rate as a function of energy cutoff for 16 g cm^{-2} polyethylene and 0, 1, 6.3, 10, and 100 g cm^{-2} of aluminum. An examination of the figure reveals that the energy cutoff does not have a significant shielding effect under these

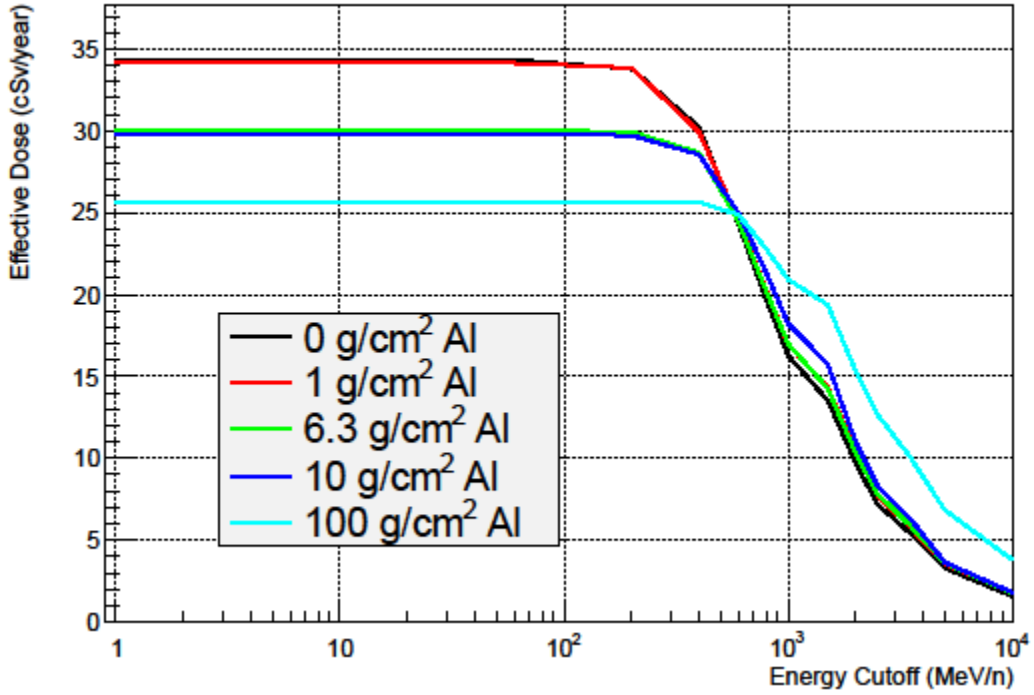

Figure 31: Effective Dose v. Cutoff Energy for Various Thicknesses of Aluminum Shielding with no Polyethylene Shielding.

combinations until energies below 200 MeV/n are cutoff. Beginning at approximately 200 MeV/n, the increase in the cutoff energy drastically reduces the effective dose, reducing the effective dose by nearly an order of magnitude between 200 and 10,000 MeV/n. However, approximately half of this benefit is obtained using a cutoff energy of 2,000 MeV/n, and additional EM shielding experiences diminishing marginal returns above this cutoff energy.

Figure 31 uses the same assumptions as Figure 30 except that no polyethylene shielding is present. Even in cases where there is no physical shielding (the black line), it appears that EM shielding is not effective unless it can block particles with energies greater than 200 MeV/n. However, above this threshold, EM shielding is quite effective at lowering the effective dose to

an astronaut. On Figure 31, comparing the relative shielding of 0 against 100 g cm^{-2} of aluminum, it appears that EM shielding blocking 600 MeV/n particles is as effective as 100 g cm^{-2} of aluminum. Furthermore, the cutoff of higher energies appears to cause aluminum to be ineffective as a shielding material above about 800 MeV/n. Above this energy, the aluminum-shielded cases generally result in higher effective dose. This effect likely occurs because many secondary particles are liberated in the aluminum by the incident high-energy particles. The aluminum is unable to stop these particles because they are so energetic. As Figure 31 shows, this is the case even when there is some polyethylene shielding behind the aluminum.

Examining the effectiveness of EM shielding when combined only with polyethylene shielding, it appears that this inversion effect also occurs for polyethylene shielding. Figure 32 shows effective dose rate as a function of cutoff energy for 0, 1, 6.3, 10, and 100 g cm^{-2} of polyethylene with no aluminum shielding present. At a cutoff energy of approximately 1000 MeV/n, it appears that the physically shielded cases actually result in a higher effective dose than the unshielded cases. As was the case with aluminum, it is likely that the presence of additional material in these cases provides the material needed to produce secondaries but is relatively ineffective at shielding high-energy incident particles. The physical shielding is effective below a cutoff energy of about 800 MeV/n.

Another interesting aspect of these effective dose calculations is revealed by an examination of some of the calculated organ dose equivalents. Figure 33 shows the effective dose and dose equivalent to the eye, skin, and blood forming organs plotted as a function of

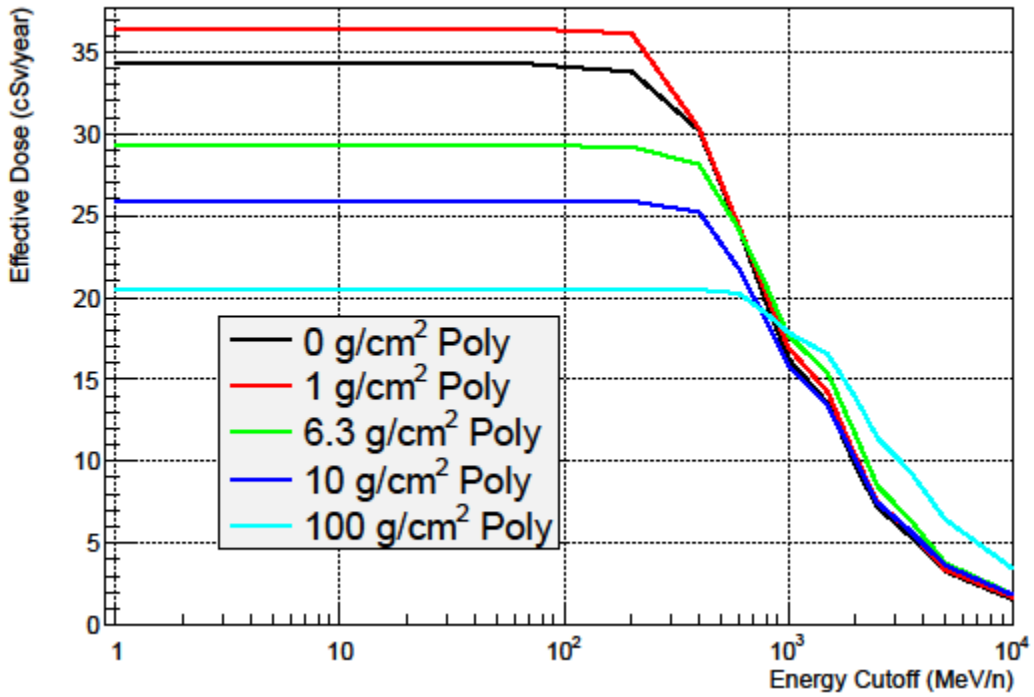

Figure 32: Effective Dose v. Cutoff Energy for Various Thicknesses of Polyethylene Shielding with no Aluminum Shielding Present.

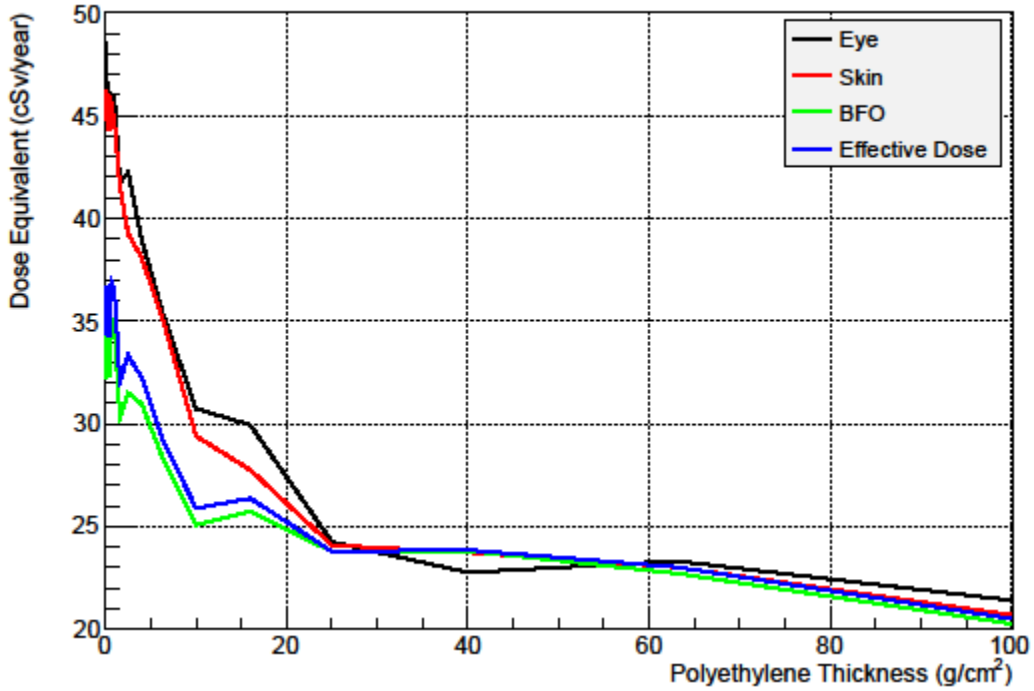

Figure 33: Effective Dose Compared to Organ Dose Equivalent to the Skin, Eyes, and Blood Forming Organs.

polyethylene thickness with no energy cutoff and no aluminum shielding. It appears that these values converge on a single value at about 25 g cm^{-2} of polyethylene shielding. This finding is consistent with the earlier observation that additional polyethylene shielding does not provide a large incremental benefit above 16 g cm^{-2}. At this point, the radiation environment past the shielding is such that the astronaut will receive the same dose equivalent throughout his or her body.

A similar calculation of effective dose for a variety of shielding calculations has been undertaken by Townsend *et al.* for shielding by the Mars atmosphere and an aluminum shield using HZETRN (Ref. 52). The FLUKA calculations do not account for the Mars atmosphere,

and the Townsend calculations do not account for polyethylene shielding. However, the results of both calculations can be compared for the case where there is exclusively aluminum shielding. A comparison of the results for the unshielded human shows that the calculations by Townsend *et al.* are 30-50% higher than the FLUKA lookup tool calculations. Several possible explanations exist for this difference. First, HZETRN and FLUKA use different physical models. Second, the FLUKA lookup tool does not include neutrons, and the neutron flux is included in the HZETRN spectrum. These differences likely account for most of the observed difference between the predictions of the two models.

Based on the above calculations, it appears that both magnetic field shielding and passive bulk shielding materials provide a level of protection against the incident GCR spectrum. In order to determine which shielding technique or combination is best-suited for use aboard a spacecraft requires a comprehensive examination of the features of each shield, including, among other things, the weight of the shield. Other factors such as the volume, reliability, and power requirements of the shield must also be considered. If two techniques provide a comparable level of protection, the shield with the lighter mass is generally preferable due to the difficulty of transporting materials into space. This work does not examine the relative size of the shielding materials in this case, and a comprehensive comparison of the relative merits of these shielding materials is not undertaken herein.

VII. Future Work and Conclusions

The FLUKA lookup tables developed for this work will provide a useful tool to NASA-JSC SRAG and other users as a means of obtain an approximate result based on pre-calculated Monte Carlo simulations. The results in the lookup tables are in good agreement with experimental data. This work also demonstrates that when the lookup tables are combined with GCR fluences calculated using BO'10, they can successfully be employed to approximate the radiation incident upon a shielded silicon detector in space. The results calculated using the lookup tables were in approximate agreement with the experimental data as well as other models created using different Monte Carlo and deterministic codes such as HETC-HEDS and HZETRN (Ref. 21). This work also demonstrated that the results calculated using the lookup table agreed closely with a simulation using FLUKA that accounted for the precise geometry and composition of CRaTER. The lookup tables were able to replicate the direct simulation closely, demonstrating the efficacy of employing lookup tables in this manner. In addition to modeling the detector, the lookup tables can be used to quickly calculate effective dose and organ dose and dose equivalent to an astronaut for a variety of different physical and electro-magnetic shielding combinations. These calculations can be easily replicated for a given SPE or GCR input spectrum to provide an approximation of the efficacy of a shielding combination aboard a spacecraft when conditions are rapidly changing. In this scenario, it would not be possible to build and run a Monte Carlo simulation of the various shielding configurations from scratch in a timely matter.

This work leaves several items for future investigation. This work only calculates the most common isotope of each ion as the incident particle. However, it is possible that the other isotopes may account for certain gaps in calculated spectrum when compared to experimental results in space. In particular, ^{2}H, ^{3}H, and ^{3}He exhibit significantly different behavior from the more abundant species, and their behavior may account for the behavior of the simulation at certain points in this comparison. Moreover, the use of energy cutoffs to simulate triple coincidence oversimplifies the behavior of the CRaTER telescope. A future calculation of the CRaTER detector using FLUKA could simulate the coincidence requirement using FLUKA's DETECT card, which enables event-by-event analysis and the application of coincidence or anti-coincidence requirements (Ref. 4). Using this approach, an isotropic GCR spectrum could be simulated, eliminating the axial incident ion assumption that are inherent in the HZETRN, HETC-HEDS, and the FLUKA models presented in this work. These additional investigations may uncover the source of the points where the existing models of CRaTER underestimate the experimental data.

Bibliography

1. NASA, 2011 NASA Strategic Plan, NP-2011-01-699-HQ.
2. K. Hurlbert, B. Bagdigian, C. Carroll, A. Jeevarajan, M. Kliss, and B. Singh, "Human Health, Life Support and Habitation Systems: Technology Area 06," NASA Space Technology Roadmaps (2012).
3. J.W. Wilson, F.F. Badavi, F.A. Cucinotta, J.L. Shinn, G.D. Badhwar, R. Silberberg, C.H. Tsao, L.W. Townsend, and R.K. Tripathi, "HZETRN: Description of a Free-Space Ion and Nucleon Transport and Shielding Computer Program." NASA TP 3495, 1995.
4. A. Ferrari, P.R. Sala, A. Fasso, and J. Ranft, "FLUKA: a multi-particle transport code," CERN-2005-10 (2005), INFN/TC_05/11, SLAC-R-773.
5. P.M. O'Neill, "Badhwar-O'Neill 2010 Galactic Cosmic Ray User Manual" (2010).
6. David W. Anderson, *Absorption of Ionizing Radiation,* Baltimore: University Park Press, (1984).
7. Gudrun Alm Carlsson, "Basic Concepts in Dosimetry. A Critical Analysis of the Concepts of Ionizing Radiation and Energy Imparted," *Radiation Research*, 75, 3, 462-470 (1978).
8. A. W. Case, J. C. Kasper, H. E. Spence, C. J. Zeitlin, M. D. Looper, M. J. Golightly, N. A. Schwadron, L. W. Townsend, J. E. Mazur, J. B. Blake, Y. Iwata, "The deep space galactic cosmic ray lineal energy spectrum at solar minimum," *Space Weather*, 11, 6, 361-368 (2013).
9. International Commission on Radiation Units and Measurements, "Fundamental Quantities and Units for Ionizing Radiation" ICRU Report 85a-Revised (2011).

10. James E. Turner (1995), *Atoms, Radiation, and Radiation Protection, Second Edition*. New York, NY: John Wiley & Sons, Inc.
11. NCRP, "Limitation of Exposure to Ionizing Radiation," Bethesda, MD, NCRP Report No. 116 (1993).
12. International Commission on Radiation Protection, "1990 Recommendations of the International Commission on Radiation Protection," *ICRP Publication 60*. Ann. ICRP 21, 1-3 (1991).
13. NCRP, "Information Needed to Make Radiation Protection Recommendations for Space Missions Beyond Low-Earth Orbit," Bethesda, MD, NCRP Report No. 153 (2006).
14. International Commission on Radiation Protection, "Recommendations of the International Commission on Radiation Protection," *ICRP Publication 26* (1977).
15. G. Battistoni, S. Muraro, P.R. Sala, F. Cerutti, A. Ferrari, S. Roesler, A. Fassò, and J. Ranft, "The FLUKA code: Description and benchmarking," Proceedings of the Hadronic Shower Simulation Workshop 2006, Fermilab 6--8 September 2006, M. Albrow, R. Raja eds., AIP Conference Proceeding 896, 31-49, (2007).
16. A. Ferrari, P.R. Sala, R. Guaraldi, and F. Padoani, "An improved multiple scattering model for charged particle transport," *Nucl. Instr. Meth.* B71, 4, 2 September 1992, p. 412-426.
17. L.W. Townsend, T.M. Miller, and T.A. Gabriel, "HETC Radiation Transport Code Development for Cosmic Ray Shielding Applications in Space", *Radiation Protection Dosimetry* 116:1-4, 135 (2005).

18. R.K. Tripathi, F.A. Cucinotta, and J.W. Wilson, “Universal Parameterization of Absorption Cross Sections: Light Systems,” NASA TP-209726 (1999).
19. L.W. Townsend, J.W. Wilson, and H.B. Bidisaria, “Heavy-Ion Total and Absorption Cross 25 MeV/Nucleon,” NASA TP- 2138 (1983).
20. L.W. Townsend, J.W. Wilson, and H.B. Bidisaria, “Nucleon and deuteron scattering cross sections from 25 MeV/Nucleon to 22.5 GeV/Nucleon,” NASA TM-84636 (1983).
21. J.A. Porter, L.W. Townsend, H. Spence, M. Golightly, N. Schwadron, J. Kasper, T. Case, J.B. Blake, J. and Mazur, C. Zeitlin, “Contributions of Primary and Secondary Particles to Observed LET for the CRaTER Instrument on LRO,” *Space Weather Journal*, submitted 2013.
22. J.H. Heinbockel, T.C. Slaba, S.R. Blattnig, R.K. Tripathi, L.W. Townsend, T. Handler, T.A. Gabriel, L.S. Pinsky, B. Reddell, M.S. Clowdsley, R.C. Singleterry, J.W. Norbury, F.F. Badavi, and S.K. Aghara,“Comparison of the Transport Codes HZETRN, HETC and FLUKA for a Solar Particle Event”, *Advances in Space Research*, 47, 6, 1079-1088 (2011).
23. T.C. Slaba, “Faster Heavy Ion Transport for HZETRN,” NASA TP-217803, 2013.
24. J.M. Brittingham, J.A. Porter, and L.W. Townsend, “Comparison of FLUKA Lookup Tables to Existing CRaTER Instrument Models,” 2013 ANS Annual Meeting. June 16-20, 2013, Atlanta, GA.
25. J. H. Heinbockel, T. C. Slaba, R. K. Tripathi, S. R. Blattnig, J. W. Norbury, F. F. Badavi, L. W. Townsend, T. Handler, T. A. Gabriel, L. S. Pinsky, B. Reddell, and A. R. Aumann.

"Comparison of the transport codes HZETRN, HETC and FLUKA for galactic cosmic rays," *Advances in Space Research*, 47, 6, 1089-1105 (2011).

26. J.D. Badhwar and P.M. O'Neill, "An improved model of GCR for space exploration mission," *Nucl. Tracks Radiation Measurement* 20, 403-10 (1992).
27. H.E. Spence, A.W. Case, M.J. Golightly, T. Hine, B.A. Larsen, J.B. Blake, P. Caranza, W.R. Crain, J. George, M. Lalic, A. Lin, M.D. Looper, J.E. Mazur, D. Dalvaggio, J.C. Kasper, T.J. Stubbs, M. Doucette, P. Ford, R. Foster, R. Goeke, D. Gordon, B. Klatt, J. O'Conner, M. Smith, T. Onsager, C. Zeitlin, L.W. Townsend, and Y. Charara, "CRaTER: The Cosmic Ray Telescope for the Effects of Radiation Experiment on the Lunar Reconnaissance Orbiter Mission," *Space Science Review*, 150, 243 (2010).
28. W.B. Christie, J.L. Romero, F.P. Brady, C.E. Tull, C.M. Castaneda, E.F. Barasch, M.L. Webb, J.R. Drummond, H.J. Crawford, I. Flores, D.E. Greiner, P.J. Lindstrom, H. Sann, and J.C. Young, "A multiple sampling ionization chamber (MUSIC) for measuring the charge of relativistic heavy ions," *Nucl. Instr. Meth.* A255, Issue 3, 1 April 1987, Pages 466-476.
29. Wyle Integrated Science and Engineering, "Develop lookup tables or parameterizations (curve fits) of particle fluences using FLUKA Monte Carlo transport code," Purchase Order No. T72057 to University of Tennessee (Nov. 30, 2010).
30. J.M. Brittingham, L.W. Townsend, J. Barzilla, and K.T. Lee, "Develop lookup tables or parameterizations (curvefits) of particle fluences using FLUKA Monte Carlo Transport Code," APS April Meeting Bulletin (2012).

31. Wyle Integrated Science and Engineering, “2012 Statement of Work for Develop lookup tables or parameterizations (curve fits) of particle fluences using FLUKA Monte Carlo transport code” (Oct. 6, 2011).
32. The University of Tennessee, Newton High Performance Computing Program, http://newton.utk.edu.
33. A. Fassò, A. Ferrari, J. Ranft, and P.R. Sala. “New developments in FLUKA modelling hadronic and EM interactions” Proc. 3rd Workshop on Simulating Accelerator Radiation Environments, KEK, Tsukuba (Japan) 7-9 May 1997. Ed. H. Hirayama, KEK Proceedings 97-5 (1997), p. 32-43.
34. James F. Ziegler, “SRIM-2003,” *Nuclear Instruments and Methods in Physics Research Section B: Beam Interactions with Materials and Atoms*, 219–220, 1027–1036 (2004).
35. P.M. O’Neill, “Badhwar-O’Neill 2010 Galactic Cosmic Ray Flux Model – Revised,” NASA TNS-00307 (2010).
36. T.C. Slaba, Cubic Interpolation Code for Badhwar-O’Neill Galactic Cosmic Ray Flux Model, unpublished.
37. Rene Brun and Fons Rademakers, “ROOT - An Object Oriented Data Analysis Framework,” Proceedings AIHENP'96 Workshop, Lausanne, Sep. 1996, Nucl. Inst. & Meth. in Phys. Res. A 389 (1997) 81-86. See also http://root.cern.ch/.
38. Hans Bichsel, “Straggling in Thin Silicon Detectors,” *Reviews of Modern Physics*, 60, 3, 663-699, (1988).
39. C. Zeitlin, “CRaTER Recalibration,” Powerpoint Presentation, 26 September 2013.

40. E.R. Benton, E.V. Benton, A.L. Frank, "Conversion between different forms of LET," *Radiation Measurements* 45 (2010) 957-59.

41. M. Golightly, "Conversion of CRaTER Detector LET_{Si} and D_{Si} to $LET_{H2O}/D_{H2O}/H$," Powerpoint Presentation, 26 June 2013.

42. J. A. Porter, L. W. Townsend, H. Spence, M. Golightly, N. Schwadron, J. Kasper, A. W. Case, J. B. Blake, J. Mazur, C. Zeitlin, "Radiation Environment at the Moon: Comparison of Transport Code Modeling and Measurements from the CRaTER Instrument," submitted.

43. Francis A. Cucinotta, Shaowen Hu, Nathan A. Schwadron, K. Kozarev, Lawrence W. Townsend, Myung-Hee Y. Kim, "Space radiation risk limits and Earth-Moon-Mars environmental models," *Space Weather*, 8, 12, S00E09 (2010).

44. L. W. Townsend, J. A. Porter, J. P. Townsend, "Comparisons of Extreme Solar Particle Event Dose Estimates on Mars to New NASA Career Limits," 2013 ANS Annual Meeting. June 16-20, 2013, Atlanta, GA.

45. F. Cucinotta, M. Kim, J. Chappel, "Space radiation cancer risks and uncertainties- 2010." National Aeronautics and Space Administration, Washington DC. NASA TP-2011-216155 (2011).

46. NCRP, "Information Needed to Make Radiation Protection Recommendations for Space Missions beyond Low-Earth Orbit," Bethesda, MD, NCRP Report No. 153 (2006).

47. L. W. Townsend, "Overview of active methods for shielding spacecraft from energetic space radiation," *Physica Medica*, 17, 84-85 (2001).

48. L. W. Townsend, "HZE Particle Shielding Using Confined Magnetic Fields," *Journal of Spacecraft and Rockets*, 20, 6, 629-630 (1983).

49. C. Zeitlin, D.M. Hassler, F.A. Cucinotta, B. Ehresmann, R.F. Wimmer-Schweingruber, D.E. Brinza, S. Kang, G. Weigle, S. Boettcher, E. Boehm, S. Burmeister, J. Guo, J. Koehler, C. Martin, A. Posner, S. Rafkin, G. Reitz. "Measurements of Energetic Particle Radiation in Transit to mars on the Mars Science Laboratory," *Science* 340, 1080 (2013).

50. M. Billings, W. Yucker, "The Computerized Anatomical Man (CAM) Model", McDonnell Douglas Company Report MDC-G465 (1973).

51. W. Yucker S. Huston, "The Computerized Anatomical Female", McDonnell Douglas Company Report MDC-6107 (1990).

52. L.W. Townsend, M. PourArsalan, F.A. Cucinotta, M.Y.Kim, N.A. Schwadron, "Transmission of galactic cosmic rays through Mars Atmosphere," *Space Weather*, 9, S00E11 (2011).

Vita

John Brittingham was born in Nashville, Tennessee and grew up both there and in Atlanta, Georgia. After graduating from high school, he attended Yale University, where he majored in physics. John then served as a submarine officer in the U.S. Navy. During his last few months in the Navy, John began work on the Master of Science in Nuclear Engineering through the University of Tennessee's distance education program, completing the program in December 2010. John also attended law school at the University of Memphis, which he completed in December 2010. He then pursued his doctorate in Nuclear Engineering at the University of Tennessee. John currently practices law in Atlanta, Georgia, where his practice concentrates on the state and federal regulation of nuclear energy.